

## Meteorological Characteristics and Overland Precipitation Impacts of Atmospheric Rivers Affecting the West Coast of North America Based on Eight Years of SSM/I Satellite Observations

PAUL J. NEIMAN, F. MARTIN RALPH, AND GARY A. WICK

*Physical Sciences Division, NOAA/Earth System Research Laboratory, Boulder, Colorado*

JESSICA D. LUNDQUIST

*Cooperative Institute for Research in the Environmental Sciences/NOAA/ESRL, Boulder, Colorado*

MICHAEL D. DETTINGER

*U.S. Geological Survey, Scripps Institution of Oceanography, La Jolla, California*

(Manuscript received 30 November 2006, in final form 22 June 2007)

### ABSTRACT

The pre-cold-frontal low-level jet within oceanic extratropical cyclones represents the lower-tropospheric component of a deeper corridor of concentrated water vapor transport in the cyclone warm sector. These corridors are referred to as atmospheric rivers (ARs) because they are narrow relative to their length scale and are responsible for most of the poleward water vapor transport at midlatitudes. This paper investigates landfalling ARs along adjacent north- and south-coast regions of western North America. Special Sensor Microwave Imager (SSM/I) satellite observations of long, narrow plumes of enhanced integrated water vapor (IWV) were used to detect ARs just offshore over the eastern Pacific from 1997 to 2005. The north coast experienced 301 AR days, while the south coast had only 115. Most ARs occurred during the warm season in the north and cool season in the south, despite the fact that the cool season is climatologically wettest for both regions. Composite SSM/I IWV analyses showed landfalling wintertime ARs extending northeastward from the tropical eastern Pacific, whereas the summertime composites were zonally oriented and, thus, did not originate from this region of the tropics. Companion SSM/I composites of daily rainfall showed significant orographic enhancement during the landfall of winter (but not summer) ARs.

The NCEP–NCAR global reanalysis dataset and regional precipitation networks were used to assess composite synoptic characteristics and overland impacts of landfalling ARs. The ARs possess strong vertically integrated horizontal water vapor fluxes that, on average, impinge on the West Coast in the pre-cold-frontal environment in winter and post-cold-frontal environment in summer. Even though the IWV in the ARs is greater in summer, the vapor flux is stronger in winter due to much stronger flows associated with more intense storms. The landfall of ARs in winter and north-coast summer coincides with anomalous warmth, a trough offshore, and ridging over the Intermountain West, whereas the south-coast summer ARs coincide with relatively cold conditions and a near-coast trough. ARs have a much more profound impact on near-coast precipitation in winter than summer, because the terrain-normal vapor flux is stronger and the air more nearly saturated in winter. During winter, ARs produce roughly twice as much precipitation as all storms. In addition, wintertime ARs with the largest SSM/I IWV are tied to more intense storms with stronger flows and vapor fluxes, and more precipitation. ARs generally increase snow water equivalent (SWE) in autumn/winter and decrease SWE in spring. On average, wintertime SWE exhibits normal gains during north-coast AR storms and above-normal gains during the south-coast AR storms. The north-coast sites are mostly lower in altitude, where warmer-than-normal conditions more frequently yield rain. During those events when heavy rain from a warm AR storm falls on a preexisting snowpack, flooding is more likely to occur.

---

*Corresponding author address:* Paul J. Neiman, Physical Sciences Division, NOAA/Earth System Research Laboratory, Mail Code R/PSD2, 325 Broadway, Boulder, CO 80305.

E-mail: paul.j.neiman@noaa.gov

DOI: 10.1175/2007JHM855.1

© 2008 American Meteorological Society

## 1. Introduction

The pre-cold-frontal low-level jet (LLJ) residing at  $\sim 1$  km MSL (e.g., Palmén and Newton 1969; Browning and Pardoe 1973; Carlson 1991) is typically part of a broader region of generally poleward heat transport within the warm sector of extratropical cyclones that is referred to as the “warm conveyor belt” (e.g., Browning 1990; Carlson 1991). The warm conveyor belt transports both sensible and latent heat, balancing the equatorward transport of comparatively cool, dry air elsewhere in the cyclone’s circulation. The latent component of the poleward heat transport, that is, the water vapor flux, can evolve differently from the sensible component, especially over oceanic regions where the sea surface serves as a major moisture source. In a maritime environment, a deep corridor of concentrated water vapor transport is often found in cyclone warm sectors and focused in the pre-cold-frontal LLJ region (Ralph et al. 2004, 2005, 2006). These corridors are referred to as atmospheric rivers because they tend to be quite narrow ( $< 1000$  km wide) relative to both their length scale ( $> \sim 2000$  km) and to the width scale of the sensible component of heat transport, and because they are responsible for almost all ( $> 90\%$ ) of the poleward water vapor transport in less than 10% of the zonal circumference at midlatitudes (Zhu and Newell 1998; Ralph et al. 2004). Consequently, these mesoscale filamentary features play a crucial role in the global water cycle and represent a key phenomenon linking weather and climate. Most ( $\sim 75\%$ ) of the water vapor transport within these rivers occurs within the lowest 2.5 km of the atmosphere, where moist-neutral stratification is also found (Ralph et al. 2005). The combination of lower-tropospheric moist neutrality, strong horizontal winds directed toward elevated terrain, and large water vapor content yields conditions that are ripe for the occurrence of heavy orographic precipitation (e.g., Rhea 1978; Smith 1979; Pandey et al. 1999; Rotunno and Ferretti 2001; Neiman et al. 2002; among others) in geographically focused regions where the narrow atmospheric rivers make landfall.

Atmospheric rivers play a critical role transporting water vapor from the eastern Pacific Ocean to western North America, resulting in significant precipitation (especially in orographically favored mountainous locales) that not only replenishes reservoirs across parts of the semiarid west but also generates devastating floods and debris flows. However, the quantitative impacts of landfalling atmospheric rivers on precipitation and flooding across western North America have only begun to be assessed. For example, Ralph et al. (2004) showed the connection between a landfalling atmo-

spheric river and a narrow swath of heavy rainfall in northern California. More recently, Ralph et al. (2006) linked heavy orographic precipitation and severe flooding in northern California’s Russian River basin to another landfalling atmospheric river. This latter study also established that all seven flood events on the Russian River between October 1997 and February 2006 coincided with atmospheric river conditions. It is becoming increasingly clear that our ability to improve predictions of many of the largest storms and floods impacting western North America, and our ability to track their progress as they propagate down the coastal margin, will depend on advancing our understanding and observations of atmospheric rivers beyond what has been presented in the studies cited above.

Though quite revealing, these studies concentrated on only a small geographic region of western North America. In contrast, this paper will explore the overland impacts of atmospheric rivers across all of western North America, from the California–Mexico border northward into British Columbia, Canada, irrespective of whether or not they produced heavy rain and/or flooding. In addition, mean synoptic characteristics and hydrologic consequences of these landfalling atmospheric rivers will be assessed. Our study focuses on eight years of atmospheric-river observations by utilizing polar-orbiting satellites as the principal observing platform for the detection of these long, narrow features, starting when daily multiple-satellite data coverage was first available regularly over the entire Pacific basin in the late 1990s. Although the significance of moisture plumes and LLJs on eastern North American weather is generally recognized, the use of multiyear satellite observations in conjunction with a dynamically consistent global reanalysis dataset (both described later) will provide new insights into our understanding of atmospheric rivers impacting the more mountainous western part of the continent.

Section 2 describes the key observing systems. The methodology for detecting and cataloging atmospheric rivers using polar-orbiting satellite data is presented in section 3. In addition, the geographic and seasonal distributions of these satellite-observed features over the eastern Pacific are addressed. Section 4 describes the synoptic-scale reanalysis tools employed to investigate the large-scale structures and dynamics of atmospheric rivers, and this section also validates the use of these tools in this endeavor. Synoptic-scale characteristics and overland impacts of atmospheric rivers (including their modulation by geographic location, season, and water vapor content) are shown in section 5. Conclusions are presented in section 6.

## 2. Observing systems

The cornerstone observing system of this 8-yr study consists of a Special Sensor Microwave Imager (SSM/I) (Hollinger et al. 1990) carried on each of four Defense Meteorological Satellite Program polar orbiters that circled the globe every  $\sim 102$  min since late 1997. The *F13* and *F14* satellites were available and utilized throughout the entire period between 1 October 1997 [start of water year (WY) 1998] and 30 September 2005 (end of WY2005). The *F11* and *F15* satellites provided additional data from 1 October 1997 to 17 May 2000 and from 23 February 2000 to 30 September 2005, respectively. Vertically integrated water vapor (IWV) (Schuessel and Emery 1990), cloud liquid water (Weng and Grody 1994), rain rate (Ferriday and Avery 1994), and ocean-surface wind speed (Goodberlet et al. 1990) were retrieved from each SSM/I sensor over a 1400-km-wide swath and were gridded at 25-km resolution. Retrievals were generally not available over land, except for the rain-rate product, which combines distinct SSM/I-only algorithms for land and ocean regions. The ocean rain-rate algorithm uses both liquid water emission and ice-scattering information, while the land algorithm uses a simple ice-scattering retrieval technique. Historically, Katsaros and Lewis (1986) and McMurdie and Katsaros (1991) were among the first to use space-based microwave IWV observations in maritime extratropical cyclone studies.

This study primarily uses the SSM/I observations of IWV and, to a lesser extent, rain-rate data. The SSM/I measurements are reliable (Wentz 1997), although IWV measurements can be degraded in heavy rain. However, because the SSM/I observations are used here solely for detecting long, narrow IWV plumes associated with atmospheric rivers (i.e., for pattern recognition) rather than for quantitative analysis, the degradation of IWV due to heavy rainfall and small inter-satellite differences does not prove detrimental. The SSM/I sampling is asynoptic and somewhat irregular in time and location. IWV and rain-rate retrievals are available at  $\sim 40$ -km native resolution from each SSM/I overpass and, for this study, were composited onto a  $0.25^\circ$  latitude–longitude grid of the ascending and descending satellite passes for each day. For the Pacific Ocean, the ascending pass composites correspond to a time interval between 0000 and 1159 UTC, and the descending pass composites range between 1200 and 2359 UTC. These 12-h ascending and descending composites provide near-complete spatial sampling of the domain. Multiple IWV and rain-rate retrievals within a grid cell were averaged, and the spatial coverage of the domain varied slightly from day to day due to the pre-

cession of the multiple orbits. Because of the similarity of the satellite orbits and their overpass times, repeated sampling of individual grid cells by the multiple satellites in the 12-h composites was constrained to a period of less than 3.5 h, thus resulting in a minimum of blurring of propagating IWV plumes. The 12-h composites were analyzed because, with daily (i.e., 24 h) compositing periods, the propagation of these narrow plumes led to significant artificial broadening and weakening of the core values of IWV. Prior to the start of WY1998, fewer satellites were available and yielded comparatively poorer composite daily spatial coverage for assessing IWV-plume characteristics. Consequently, those earlier years were not included in the SSM/I data analysis.

Additional datasets used in this study are as follows. California's Department of Water Resources manages a network of automatic snow-monitoring stations throughout the Sierra Nevada, and the U.S. Department of Agriculture's Natural Resources Conservation Service manages a similar network across the rest of the western United States. Snow pillows at these sites measure the weight of the snow accumulation and thereby the snow water equivalent (SWE) of the snowpack. The snow pillows report information at hourly intervals, but because pillows can experience several hours of delay in responding to changes in SWE (Beaumont 1965; Trabant and Clagett 1990), daily averages are used here. Most changes in SWE represent snow accumulation or melting. Most snow pillows are located in flat meadows with surrounding forested areas that shelter the pillow from wind scouring (Farnes 1967). Compared to nearby forested areas, these sites tend to accumulate more snow but are also more exposed to sunlight during the melt season. Most of these stations have collocated rain gauges, which measure accumulated precipitation. Rain gauges from the National Weather Service's (NWS) Automated Local Evaluation in Real Time (ALERT; Mendell 1992) network are also used. Finally, the NWS's Cooperative Observer Program (COOP) provides observations from a dense network of volunteers who report daily maximum and minimum temperatures and precipitation, generally with ventilated thermometers and storage precipitation gauges located in level, open clearings.

## 3. SSM/I IWV and rainfall plumes

### a. Method of detection

Although the satellite-observed SSM/I data alone cannot quantify moisture transport due to a lack of wind direction information at the surface and a lack of any wind data aloft, Ralph et al. (2004) established the

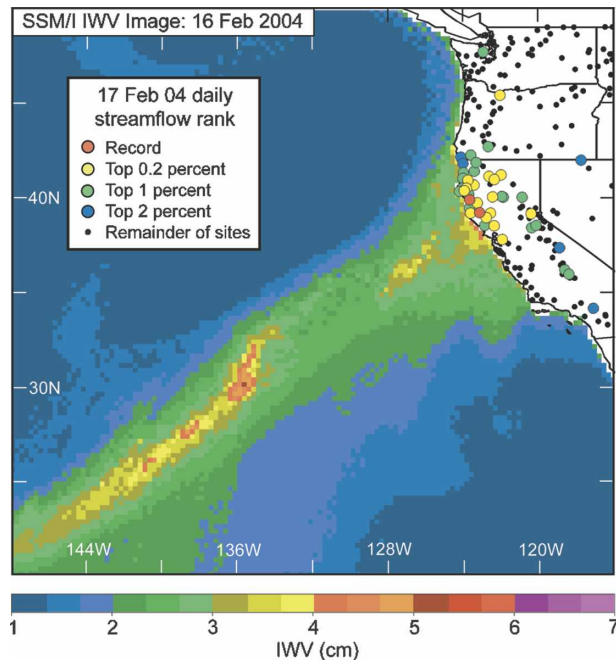


FIG. 1. Composite SSM/I satellite image of IWV (cm; color bar at bottom) constructed from polar-orbiting swaths between  $\sim$ 1400 and 1830 UTC 16 Feb 2004 and ranking of daily streamflows (percent; see inset key) on 17 Feb 2004 for those gauges that have recorded data for  $\geq 30$  yr. The streamflow data are based on local time; add 8 h to convert to UTC. From Ralph et al. (2006).

value of using the IWV as a proxy for atmospheric-river detection over the eastern Pacific during a single winter. Under this approach, narrow plumes of SSM/I IWV with values  $> 2$  cm that were  $> 2000$  km long and  $< 1000$  km wide were defined as atmospheric rivers. The present study will apply the same criteria in the same region, but for the eight water years since the daily SSM/I data were available reliably, and with the added constraint that the IWV plumes intersected the west coast of North America between  $32.5^\circ$  and  $52.5^\circ$ N latitude. Because the SSM/I products do not directly measure horizontal transport of water vapor, but instead indicate the presence of water vapor concentrations, these plumes are described in this section as plumes rather than atmospheric rivers. In a subsequent section (i.e., section 4c), the close correspondence between the plumes and atmospheric rivers will be demonstrated.

To explore the relationship between the geographic location of landfalling IWV plumes and their mean synoptic characteristics and overland precipitation impacts, IWV plumes in the eight years of SSM/I data were stratified into two groups: those making landfall in California (i.e.,  $32.5^\circ$ – $41.0^\circ$ N) and those intersecting the coast farther north in Oregon, Washington, and/or British Columbia (i.e.,  $41.0^\circ$ – $52.5^\circ$ N). These subdomains are hereafter referred to as the south-coast and north-

coast domains, respectively. Only those IWV plumes making landfall during both the ascending and descending SSM/I composites for a given day in the given domain were included in the respective group. The south–north stratification was carried out in recognition of the fact that the climatology of landfalling storms may be quite different in these domains. Figure 1 shows an example of an IWV plume impacting the south-coast domain during the descending SSM/I composite on 16 February 2004 [see Ralph et al. (2006) for further details on this case]. An additional tier of stratification was performed for the diametrically opposed winter and summer seasons to assess fundamental similarities and differences of IWV-plume characteristics based on the time of year they were observed. Winter is defined here as December–February (DJF), and summer is June–August (JJA). Finally, the wintertime SSM/I observations were stratified based on the magnitude of IWV within the core of the plumes to determine the dynamical variability associated with wintertime IWV plumes with differing water vapor content. Specifically, in addition to the 2-cm threshold described above, an additional class of strong wintertime IWV plumes with coherent regions of IWV  $> 3$  cm within 1000 km of the coast (as in Fig. 1) was categorized and analyzed.

#### b. Geographic and seasonal distributions

The north-coast region experienced nearly 3 times as many days with landfalling IWV plumes exceeding 2 cm as the south coast during the water years 1998–2005: 301 versus 115 (Tables 1 and 2). The seasonal distributions also differ markedly between the domains (Fig. 2). In the south-coast region, a broad maximum of IWV-plume events span the months between October and March, corresponding to enhanced baroclinic cyclogenesis typical of the cool season over the North Pacific basin. A secondary IWV-plume maximum occurs during May and June, while during July through September (i.e., the climatological dry season) the south coast receives very few plumes. In contrast, the greatest number of IWV plumes arrives in the north coast during the summer and autumn, with comparatively fewer episodes in early winter, and fewest between February and April. This north-coast seasonal pattern occurs despite the fact that—as is also the case in the south-coast domain—the cool season is the climatologically wettest period in the north. IWV plumes impact the south coast more than twice as often as the north coast during February and March, consistent with the fact that the climatological storm track is at its southernmost position then.

Plan-view composites of IWV, averaged over days when plumes were arriving on the north and south

TABLE 1. Dates (year, month, day) of long, narrow SSM/I IWV plumes with core values  $>2$  cm intersecting the Oregon/Washington/ British Columbia coast ( $41.0^{\circ}$ – $52.5^{\circ}$ N) during the water years 1998–2005. Only those plumes making landfall during both the morning ascending SSM/I passes and the afternoon descending passes for a given date are included in the list. The bold dates denote strong wintertime cases with coherent regions of IWV  $>3$  cm in either the morning or afternoon passes. The asterisk (\*) indicates dates included in the winter (DJF) composites; # indicates dates included in the summer (JJA) composites.

Number	WY1998	WY1999	WY2000	WY2001	WY2002	WY2003	WY2004	WY2005
1	19971001	19981005	19991008	20001001	20011010	20021003	20031006	20041006
2	19971015	19981006	19991013	20001008	20011104	20021027	20031016	20041008
3	19971016	19981012	19991017	20001017	20011109	20021106	20031017	20041011
4	19971026	19981017	19991030	20001022	20011114	20021112	20031018	20041012
5	19971029	19981113	19991103	20001023	20011115	20021119	20031019	20041015
6	19971030	19981114	19991106	20001123	20011119	<b>20021212*</b>	20031020	20041016
7	19971031	19981121	19991111	20010430	<b>20020106*</b>	20030102*	20031021	20041022
8	19971102	19981125	19991112	20010606#	<b>20020107*</b>	<b>20030126*</b>	20031022	20041102
9	19971103	19981228*	19991113	20010620#	20020221*	20030131*	20031027	20041105
10	19971105	19981229*	19991114	20010703#	20020413	20030313	20031129	20041106
11	19971216*	19990110*	19991125	20010707#	20020604#	20030523	20040122*	20041107
12	19971228*	<b>19990114*</b>	<b>19991215*</b>	20010709#	20020625#	20030524	20040526	20041108
13	<b>19980123*</b>	19990224*	19991216*	20010802#	20020626#	20030527	20040706#	20041115
14	19980322	19990227*	20000521	20010803#	20020627#	20030626#	20040712#	20041124
15	19980609#	19990511	20000522	20010805#	20020706#	20030709#	20040717#	20041125
16	19980614#	19990531	20000523	20010821#	20020710#	20030711#	20040718#	20041208*
17	19980615#	19990604#	20000527	20010822#	20020715#	20030712#	20040729#	20041209*
18	19980624#	19990623#	20000607#	20010825#	20020716#	20030714#	20040803#	<b>20041210*</b>
19	19980706#	19990628#	20000612#	20010828#	20020717#	20030720#	20040804#	<b>20041211*</b>
20	19980712#	19990629#	20000614#	20010830#	20020718#	20030818#	20040817#	20041217*
21	19980713#	19990720#	20000617#	20010901	20020723#	20030821#	20040820#	<b>20050117*</b>
22	19980714#	19990726#	20000630#	20010903	20020725#	20030825#	20040821#	20050118*
23	19980715#	19990728#	20000718#	20010910	20020728#	20030831#	20040828#	20050119*
24	19980716#	19990729#	20000719#	20010912	20020729#	20030903	20040829#	<b>20050122*</b>
25	19980717#	19990802#	20000720#	20010921	20020730#	20030904	20040830#	20050123*
26	19980723#	19990817#	20000727#	20010922	20020808#	20030905	20040831#	20050327
27	19980724#	19990818#	20000728#	20010923	20020809#	20030906	20040910	20050416
28	19980809#	19990819#	20000729#		20020822#	20030911	20040911	20050514
29	19980812#	19990821#	20000730#		20020823#	20030914	20040915	20050515
30	19980813#	19990822#	20000731#		20020828#	20030918	20040922	20050629#
31	19980827#	19990823#	20000817#		20020829#	20030922	20040925	20050704#
32	19980830#	19990824#	20000818#		20020901	20030923		20050705#
33	19980901	19990825#	20000823#		20020902	20030925		20050708#
34	19980902	19990826#	20000824#		20020910			20050716#
35	19980903	19990827#	20000825#		20020911			20050727#
36	19980907	19990828#	20000829#		20020912			20050728#
37	19980908	19990829#	20000907		20020916			20050730#
38	19980911	19990904	20000910					20050731#
39	19980913	19990905	20000917					20050801#
40	19980924	19990923	20000918					20050805#
41		19990929	20000920					20050817#
42			20000929					20050820#
43			20000930					20050821#
44								20050822#
45								20050826#
46								20050827#
47								20050908
48								20050929
49								20050930

coasts, were constructed for winter and summer (Figs. 3a–d) to gauge the mean geographic and seasonal variability of IWV plumes impacting the West Coast. The winter composites are composed of 29 and 35 dates for the north- and south-coast domains, respectively, while

the summer composites contain 133 dates in the north and 15 dates in the south. Both winter composites show an IWV plume originating from the tropical water vapor reservoir in the eastern Pacific and extending northeastward to the respective coastlines. The average

TABLE 2. Dates (year, month, day) of long, narrow SSM/I IWV plumes with core values >2 cm intersecting the California coast (32.5°–41.0°N) during the water years 1998–2005. Only those plumes making landfall during both the morning ascending SSM/I passes and the afternoon descending passes for a given date are included in the list. The bold dates denote strong wintertime cases with coherent regions of IWV >3 cm in either the morning or afternoon passes. The asterisk (\*) indicates dates included in the winter (DJF) composites; # indicates dates included in the summer (JJA) composites.

Number	WY1998	WY1999	WY2000	WY2001	WY2002	WY2003	WY2004	WY2005
1	19971002	19981108	19991014	20010328	20011011	20021107	20031005	20041009
2	19971009	19981121	19991026	20010515	20011030	20021108	20031109	20041018
3	19971029	19981123	19991028	20010516	20011116	20021109	20031129	20041026
4	19971031	19990115*	19991110	20010605#	20011122	<b>20021213*</b>	20031130	20041227*
5	19971106	19990207*	19991111	20010625#	20011129	<b>20021214*</b>	<b>20031205*</b>	20050109*
6	19971119	19990324	19991115	20010626#	20011202*	<b>20021216*</b>	20031206*	20050110*
7	19971125	19990325	20000116*	20010627#	<b>20011229*</b>	20021227*	20031207*	20050322
8	<b>19971205*</b>	19990511	<b>20000117*</b>	20010730#	20020102*	20030112*	20031224*	20050504
9	19971214*	19990802#	<b>20000118*</b>	20010925	<b>20020106*</b>	20030113*	<b>20040216*</b>	20050508
10	19980114*	19990830#	<b>20000124*</b>	20010926	20020414	20030212*	20040217*	20050515
11	19980115*		<b>20000125*</b>		20020529	20030310	20040527	20050516
12	19980126*		20000305		20020618#	20030315	20040528	20050519
13	<b>19980202*</b>		20000417			20030323	20040911	20050522
14	<b>19980203*</b>		20000507			20030326	20040917	20050608#
15	<b>19980205*</b>		20000508			20030908		20050609#
16	19980322		20000523					20050617#
17	19980323		20000612#					20050709#
18	19980525							20050710#
19	19980625#							

core values of IWV surpass the 2-cm threshold only marginally due to the averaging of many narrow plumes with differing positions and orientations. The averaged core values in the summertime IWV composites are greater than those observed during the winter, despite the fact that summer is the climatological dry season for

both coastal domains. The summertime composited IWV plumes are broader than the wintertime composites, indicating less event-to-event geographic consistency. In addition, the summertime plumes do not originate from the tropical eastern Pacific, and the averaged IWV plumes for both domains are more zonally ori-

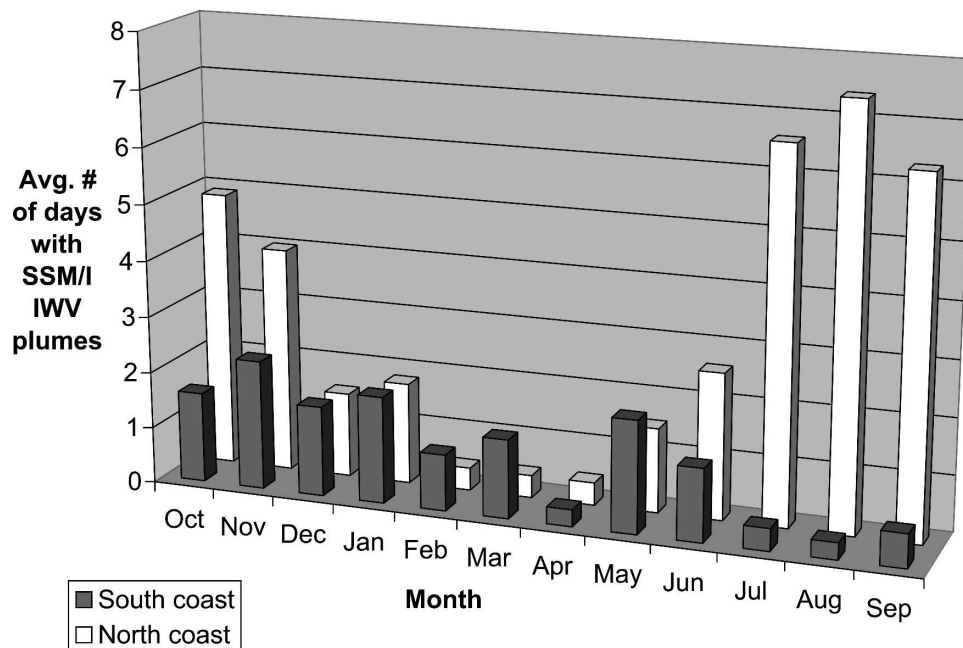


FIG. 2. Monthly distribution of the average number of days SSM/I-observed IWV plumes intersected the north-coast and south-coast domains during the water years 1998–2005.

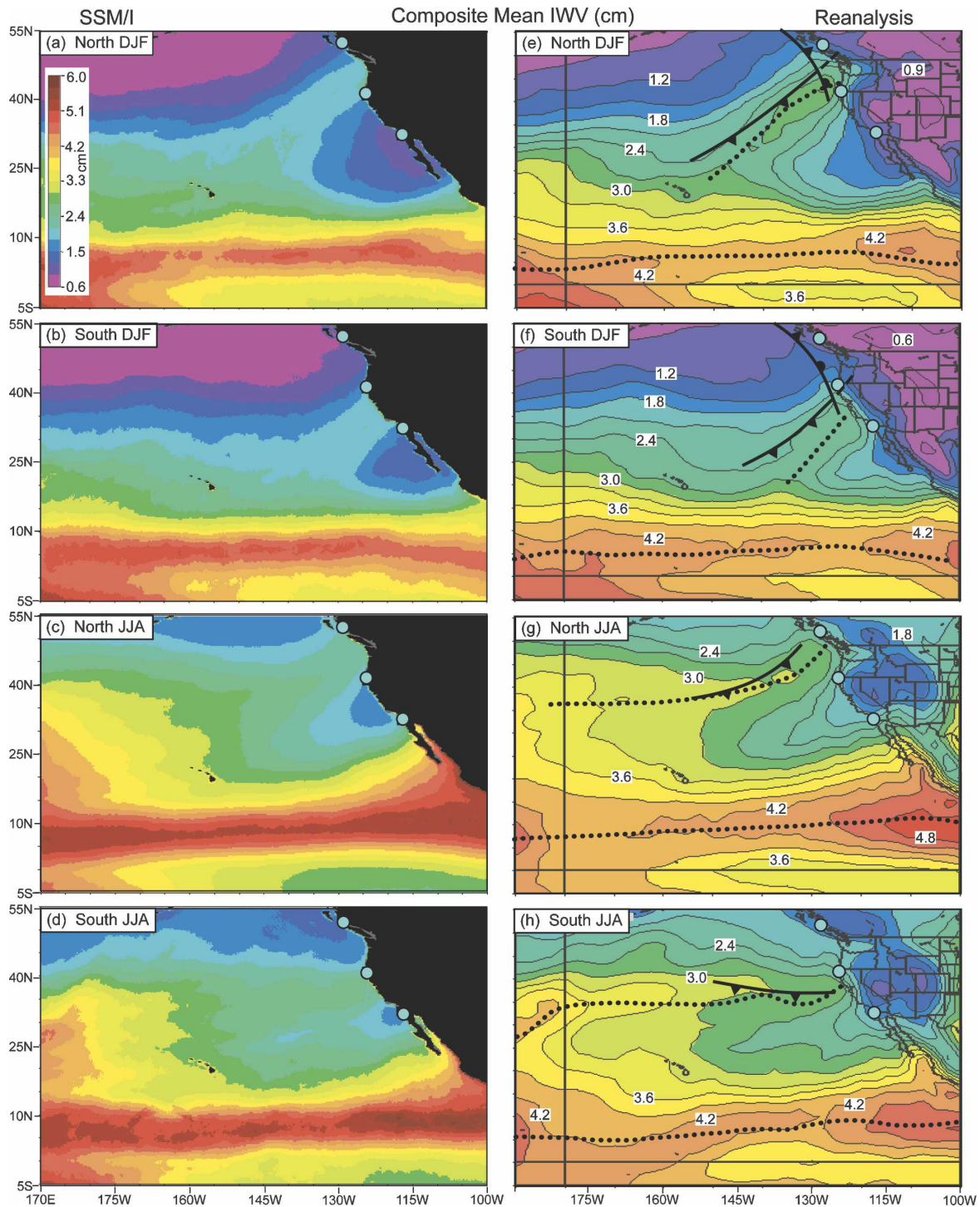


FIG. 3. Composite IWV (cm) mean fields based on SSM/I IWV plumes intersecting the north-coast and south-coast domains on a daily basis (i.e., from 0000 to 0000 UTC) in winter and summer: SSM/I observations for (a) north-winter, (b) south-winter, (c) north-summer, and (d) south-summer; and NCEP–NCAR daily reanalyses for (e) north-winter, (f) south-winter, (g) north-summer, and (h) south-summer. Panel (a) contains the color scale for the SSM/I observations, which approximately matches the reanalysis scale. The bold light-blue dots along the coast denote the boundaries of the north-coast and south-coast domains. The bold dotted lines in (e)–(h) mark the axes in the core of the IWV plumes and ITCZ observed in (a)–(d). Standard frontal notation in (e)–(h) is used to mark the composite near-surface frontal positions; the bold dashed frontal lines near the coast in (e) and (f) mark the approximate positions of the polar cold front above the occlusion. All reanalysis figures were generated using the NOAA–CIRES Climate Diagnostics Center (now ESRL) online products.

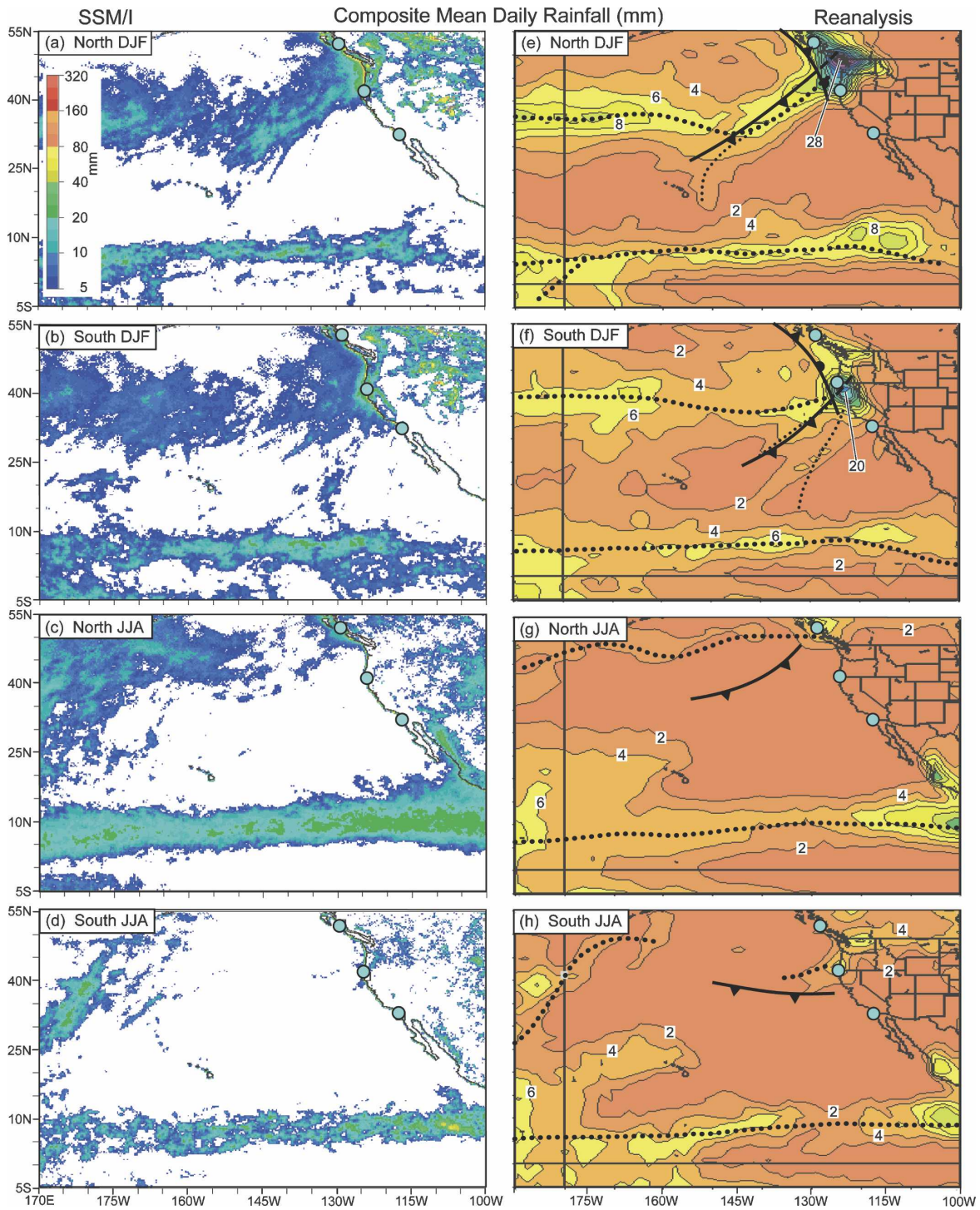


FIG. 4. Same as in Fig. 3, but for daily rainfall (mm). The color bar in (a) is valid for the panels in the left column only. The thin dotted lines in (e) and (f) mark the axes of precipitation features extending toward the tropics.

ented than their wintertime counterparts. The summer composites also show a northward protrusion of enhanced IWV along the west coast of Mexico associated with the North American monsoon (Higgins et al. 2006).

Companion SSM/I daily rainfall composites are shown in Figs. 4a–d. The wintertime rainfall enhancements extend southwestward from the coast in a broad band, then westward across the entire eastern Pacific basin. The cross-Pacific rainbands are joined by nar-

rower precipitation filaments that extend southwestward toward the tropics east of the Hawaiian Islands. Nearshore, orographic precipitation enhancement is evident within several hundred kilometers of the coast in both wintertime composites. These composite analyses support the case-study findings by Ferraro et al. (1998) that prominent IWV plumes often appear to be linked to significant rain events. The north-coast composite also exhibits significant coastal precipitation during south-coast IWV-plume events, although the opposite is not true, which is consistent with the fact that the Pacific Northwest is climatologically wetter than California during winter. The summertime composites portray rainfall distributions that are fundamentally different from their wintertime counterparts. Namely, the offshore precipitation band and coastal orographic enhancement are weakly defined in the northern composite and absent in the southern one, despite the fact that the corresponding IWV plumes contain greater water vapor content during the summer. The south-coast summer rainfall composite contains scattered precipitation across interior Oregon and Washington, but the sample size (15) is small. Because the south-coast domain recorded the greatest number of IWV plume events in November and May, separate south-coast rainfall composites were generated for those two months (not shown). Both monthly rainfall composites mirror the adjacent seasonal composites, although November is slightly drier than winter and May slightly wetter than summer. All four seasonal composites highlight the precipitation associated with the intertropical convergence zone (ITCZ; Waliser and Somerville 1994), and the summertime panels show the monsoon precipitation over western Mexico. The notably more dense and broad ITCZ pattern in the north-summer composite arises due to the averaging of approximately 4–9 times as many cases than for the other composites.

#### 4. IWV and rainfall plumes in the NCEP–NCAR reanalysis database

##### a. Description and compositing methodology

The large-scale conditions associated with landfalling IWV plumes were gauged by constructing composite synoptic-scale mean and anomaly<sup>1</sup> fields using the coarse ( $\sim 2.5^\circ$  latitude  $\times$   $\sim 2.5^\circ$  longitude) daily global

<sup>1</sup> Each reanalysis anomaly field presented in this paper was obtained by first calculating the desired composite mean field using the dates specified in Tables 1 and 2, and then subtracting from that mean field the long-term, Web-based average based on those same dates for all years in the 29-yr inclusive period between 1968 and 1996.

gridded dataset from the National Centers for Environmental Prediction–National Center for Atmospheric Research (NCEP–NCAR) reanalysis project (Kalnay et al. 1996). Four sets of plan-view reanalysis composites were created, using those dates when IWV plumes with core values  $>2$  cm intersected the north-coast and south-coast domains during the winter and summer months (see Tables 1 and 2 for the lists of dates). Those same dates were used to construct reanalysis-based, composite-mean thermodynamic and wind profiles at representative north- and south-coast locations [i.e., at Cape Flattery, Washington ( $48.38^\circ\text{N}$ ,  $124.71^\circ\text{W}$ ), and Bodega Bay, California ( $38.31^\circ\text{N}$ ,  $123.07^\circ\text{W}$ ), respectively] utilizing all available plan-view reanalysis levels from the surface upward to 300 hPa. Two additional sets of plan-view reanalysis composites were generated based on those days when IWV plumes with the greatest water vapor content (i.e.,  $>3$  cm) crossed the north- and south-coast domains during the winter months (Tables 1 and 2). It should be noted that the global reanalysis dataset used in this study does not include SSW/I IWV data.

##### b. Validation using SSM/I observations

In an effort to assess the extent to which the coarsely gridded reanalysis composites captured the prominent features observed by SSM/I, the IWV and rainfall fields from these two data sources are presented together in Fig. 3 and 4, and axes of maximum IWV and rainfall observed by SSM/I are overlaid on the appropriate reanalysis fields. The reanalysis composites accurately depict the position and orientation of the composite IWV plumes and their precipitation distributions observed by SSM/I. In addition, the wintertime reanalysis composites capture the narrow SSM/I-observed precipitation filaments east of Hawaii that join the primary precipitation band. Finally, the tropical water vapor reservoir and its ITCZ-generated precipitation are clearly represented in the reanalysis composites. The near-surface fronts portrayed on the reanalysis panels will be discussed in section 5a.

The magnitude of IWV within the core of the composite plumes is smaller in the fine-resolution ( $\sim 25$  km) SSM/I panels than their coarse-resolution ( $\sim 250$  km) reanalysis counterparts, largely because there was less spatial overlap of the very narrow SSM/I IWV plumes from case to case than the broader-scale reanalysis plumes. Hence, the averaging of the many IWV plumes resulted in a greater reduction within the core of the composite SSM/I plumes than the composite reanalysis plumes. Meanwhile, the magnitude of orographically enhanced precipitation near the coast is greater in the SSM/I, because the satellite-based observations are ca-

pable of detecting finescale, terrain-anchored precipitation that is poorly resolved in the reanalysis. Although the coarse gridding of the reanalysis dataset only marginally resolves the width of the IWV plumes and does not fully resolve the orographic precipitation, the overall favorable comparisons between the SSM/I and reanalysis composites (Figs. 3 and 4) indicate that the reanalysis dataset describes the larger-scale conditions under which the IWV plumes form and propagate. Thus, we will use the reanalysis composites to explore the larger-scale dynamical attributes associated with these plumes.

### c. *The link between SSM/I IWV plumes and atmospheric rivers*

The long, narrow SSM/I IWV plumes described above are suggestive of atmospheric rivers, which account for >90% of the meridional water vapor transport in <10% of the global circumference at midlatitudes (e.g., Zhu and Newell 1998; Ralph et al. 2004, 2005). To quantitatively evaluate whether these plumes are indeed atmospheric rivers (i.e., whether they are corridors along which vapor transport is especially concentrated), the vapor transports associated with IWV plumes impacting the west coast of North America were analyzed using the daily NCEP–NCAR reanalysis dataset. For this analysis, vertically integrated horizontal water vapor fluxes [hereafter, integrated vapor transport (IVT)] were calculated from the water vapor mixing ratios ( $q$ ) and zonal and meridional wind components ( $u$  and  $v$ , respectively) at the surface and on all mandatory-level pressure surfaces ( $p$ ) up to 300 hPa. The product components  $\bar{q} \times \bar{u} \times dp/g$  and  $\bar{q} \times \bar{v} \times dp/g$  (overbars denote mean values within each adjacent pressure layer  $dp$ , and  $g$  is gravitational acceleration) at each grid point were summed vertically from the earth's surface to 300 hPa and then combined into a horizontal transport vector, with units of  $\text{kg m}^{-1} \text{s}^{-1}$ .

Plan-view composited mean and anomaly IVT fields for the winter and summer IWV-plume events intersecting the north- and south-coast domains are presented in Fig. 5 (these, and all subsequent plan-view reanalyses, cover a smaller domain than in Figs. 3 and 4). Clearly, the IWV plumes for all four composites are associated with anomalously strong corridors of vapor transport impinging on the West Coast, thus highlighting the fact that the plumes are indeed atmospheric rivers [as was first suggested by Ralph et al. (2004)]. The wintertime atmospheric rivers, in the mean, transport considerably more water vapor to the coast than their summertime counterparts, despite the fact that the IWV content is greater in the summertime rivers (e.g., Fig. 3). This situation arises because the winter

storms possess much stronger winds. The strongest transports occur, on average, in the north-coast winter events. The reanalysis estimates of IVT in the core of the composite wintertime atmospheric rivers ( $\sim 350\text{--}550 \text{ kg s}^{-1} \text{ m}^{-1}$ ) are comparable to dropsonde observations in atmospheric rivers over the eastern Pacific (Ralph et al. 2004, 2005). Significantly, the composite wintertime rivers include a substantial meridional transport component that extends northward from the tropics (<30°N) to the coast. In contrast, the composite north-coast summertime river is zonally oriented, and the composite south-coast summertime river transports water vapor east-southeastward to the coast. The dynamical conditions responsible for these differing characteristics will be explored next.

## 5. Synoptic characteristics and overland impacts of atmospheric rivers

### a. *Geographic and seasonal variability*

#### 1) METEOROLOGICAL CHARACTERISTICS

A composite representation of the near-surface fronts that affected the West Coast during the landfall of SSM/I IWV plumes was derived from distinct features in the reanalysis composite 925-hPa fields and is shown on the reanalysis panels in Figs. 3–5. For the wintertime reanalysis IWV composites (Figs. 3e,f), the averaged IWV plume is situated on the warm side of a polar cold front and extends northeastward from the open ocean to a coast-parallel occlusion that quite likely developed due to terrain effects (Bergeron 1937); the averaged plume reaches land east of the occlusion on the warm side of the cold front aloft. The corresponding IVT composites (Figs. 5a,b) show that the region of maximum vapor transport associated with wintertime atmospheric river conditions is also on the warm side of the front. These composite results mirror a wintertime case study of a pre-cold-frontal landfalling atmospheric river that generated significant flooding in northern California (Ralph et al. 2006). The composite rainfall reanalyses (Figs. 4e,f) show a primary band of precipitation along the cold front that ultimately extends westward behind the cold front and beyond the date line, and a secondary band of warm-sector precipitation extending from the tropics toward the front. The western portion of the primary precipitation band (i.e., west of  $\sim 145^\circ\text{W}$  and north of  $\sim 30^\circ\text{N}$ ) exhibits a separate maximum that is quite likely tied to warm advection in advance of the next storm system (based on the inspection of the composite temperature and wind fields). Along the coast, the core of orographically enhanced coastal precipitation occurs in pre-cold-frontal

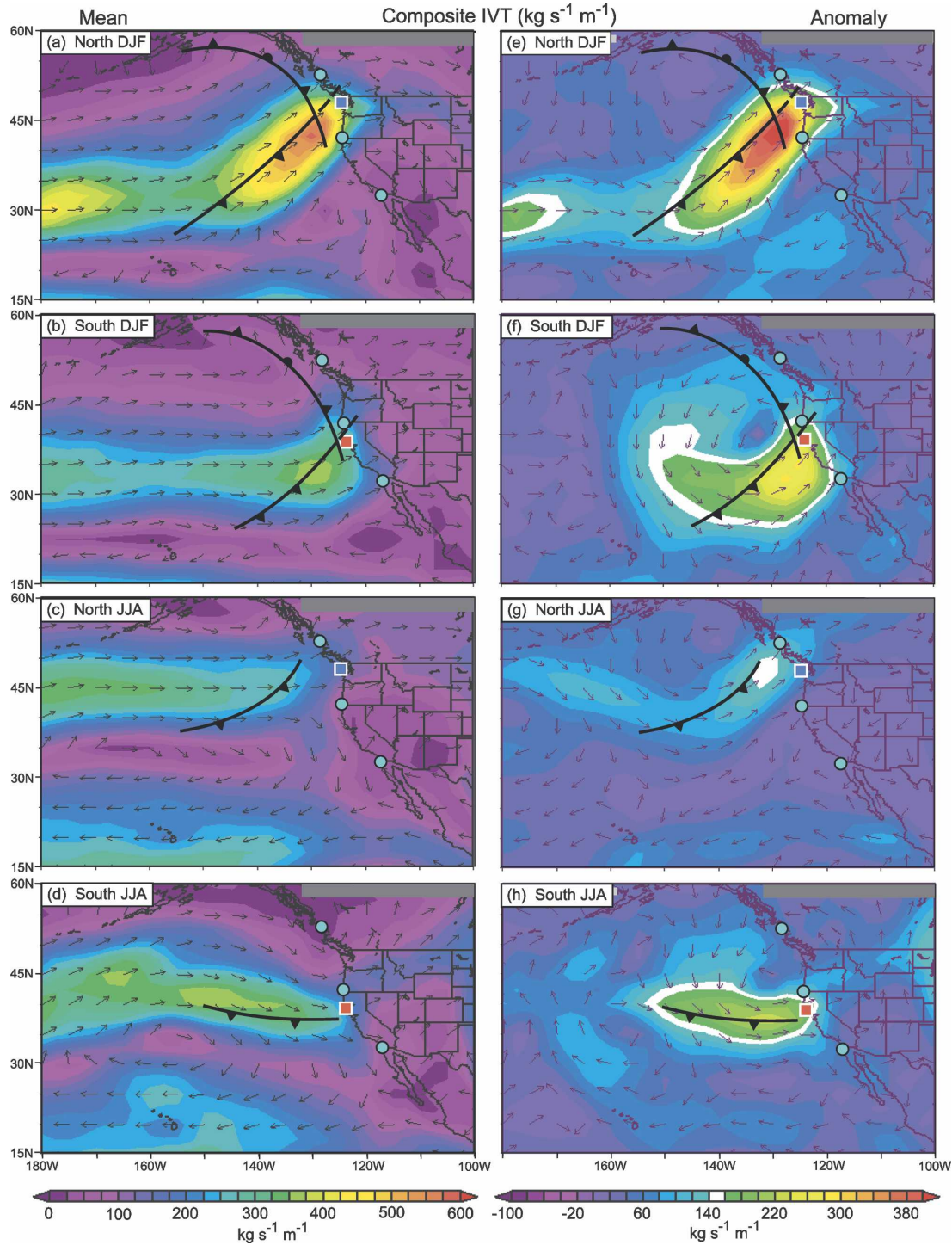


FIG. 5. Composite vertically integrated horizontal water vapor flux (IVT;  $\text{kg s}^{-1} \text{m}^{-1}$ ) derived from the NCEP–NCAR daily reanalysis dataset for SSM/I IWV plumes intersecting the north-coast and south-coast domains on a daily basis (0000–0000 UTC) in winter and summer: means for (a) north-winter, (b) south-winter, (c) north-summer, and (d) south-summer; and anomalies for (e) north-winter, (f) south-winter, (g) north-summer, and (h) south-summer. The vectors show the direction of IVT. The fronts and bold light-blue dots are as in Fig. 3. In each panel, the blue (red) square in the north- (south-) coast domain marks the position of NCEP–NCAR reanalysis thermodynamic/wind profiles presented in Fig. 10.

conditions aloft. The summertime IWV-plume counterparts are also associated with advancing polar cold fronts (Figs. 3g,h), although these fronts and their associated IVT maxima (i.e., atmospheric rivers; Figs. 5c,d) are weaker than during winter. The summertime atmospheric rivers reside on the cold side of the cold front, as does most of the precipitation (Figs. 4g,h), even though the IWV maximum in the north-coast composite extends into the prefrontal environment.

To further quantify the synoptic conditions associated with atmospheric rivers impacting the north and south coasts during winter and summer, additional reanalysis composites were constructed. Mean 500-hPa geopotential height analyses for winter (Figs. 6a,b) portray a trough over the eastern Pacific and broad southwesterly flow crossing the coast. The corresponding anomaly fields (Figs. 6e,f) show a prominent couplet, although the magnitude of the north-coast negative anomaly offshore is slightly less than that of the positive anomaly over the western United States ( $-110$  versus  $+130$  m); the opposite weighting holds in the south coast ( $-170$  versus  $+80$  m). The summertime north-coast composites (Figs. 6c,g) are qualitatively similar to their winter counterparts, although the trough-ridge couplet is much weaker in amplitude. In contrast, the summertime south-coast composites (Figs. 6d,h) are decidedly different from the others; the trough axis and associated negative anomaly are on the West Coast rather than offshore. Mean 925-hPa height fields (Fig. 7) generally reflect the characteristics observed aloft at 500 hPa. Notably, in summer, the relatively strong, zonally elongated 925-hPa anticyclone centered north of Hawaii effectively precludes the direct transport of low-level tropical moisture northward into the pre-cold-frontal environment. In winter, by contrast, a more circular composite 925-hPa anticyclone is displaced southeastward, so that it is more conducive to poleward transport of water vapor from the tropics to the West Coast in advance of the cold fronts.

Reanalysis temperature composites at 925 hPa (Fig. 8) highlight the mean low-level frontal baroclinicity and below-normal temperatures in the post-cold-frontal environment in all four atmospheric river regimes. The composites also depict anomalously warm conditions in the pre-cold-frontal domain along the north coast during both seasons and along the south coast in winter. These above-normal temperatures extend well inland (conforming to large positive anomalies observed with the NWS COOP network; not shown) and far offshore. The wintertime temperature anomalies (and their geopotential height counterparts in Figs. 6 and 7) are similar to those presented in Lackmann and Gyakum (1999) and Pandey et al. (1999) for heavy cool-season

precipitation events in the Pacific Northwest and California, respectively, thus suggesting that those storms may have been associated with atmospheric rivers. As with the geopotential height composites, the temperature composites for the south-coast summer (Figs. 8d,h) are fundamentally different from the others. Specifically, below-normal temperatures cover the entire south-coast domain, likely because the geopotential troughs aloft moderated the normally warm low-level air masses found over the western United States during summer.

Companion vertical velocity ( $\omega$ ) composites at 600 hPa (Fig. 9)—that is, near the climatological level of nondivergence for synoptic-scale weather systems (e.g., Carlson 1991)—portray distributions of ascent that closely match the rainfall fields (Fig. 4). In both winter composites (Figs. 9a,b), ascent is maximized where the composite atmospheric rivers (Figs. 5a,b) reach the coast ahead of the cold fronts aloft. In addition, organized upward motion over the eastern Pacific parallels each composite cold front, and a band of ascent arcs northwestward to the Gulf of Alaska with each composite occluded front. Subsidence accompanies the mean midtropospheric ridge across the southwestern United States. In contrast to the winter composites, the north-coast summer  $\omega$  composite (Fig. 9c) exhibits a much weaker ascent maximum at the coast and neutral vertical motion along the composite cold front offshore. The south-coast summer composite (Fig. 9d) shows a weak  $\omega$  maximum shifted inland from the coast and subsidence rather than ascent along the cold front over the eastern Pacific. The conspicuous lack of ascent along the composite cold front in the summer analyses arises because summertime cold fronts are, on average, dynamically weaker than their wintertime counterparts and because a quasi-permanent subtropical anticyclone over the eastern Pacific during summer generates a broad region of subsidence. This subsidence acts in tandem with cold eastern Pacific sea surface temperatures to generate a strong inversion that suppresses vertical motions. The lack of uplift is consistent with the relatively light precipitation tied to West Coast atmospheric rivers in summer.

Reanalysis-based winter and summer profiles at Cape Flattery, Washington (north coast), and Bodega Bay, California (south coast) (Fig. 10), provide additional dynamical information related to atmospheric rivers and their landfalling impacts. As expected, the summer profiles are warmer and contain more water vapor than their winter counterparts (Figs. 10a–c). The south-coast profiles are also warmer and contain more water vapor than the north-coast profiles. Although water vapor content is greater in summer, the summer-

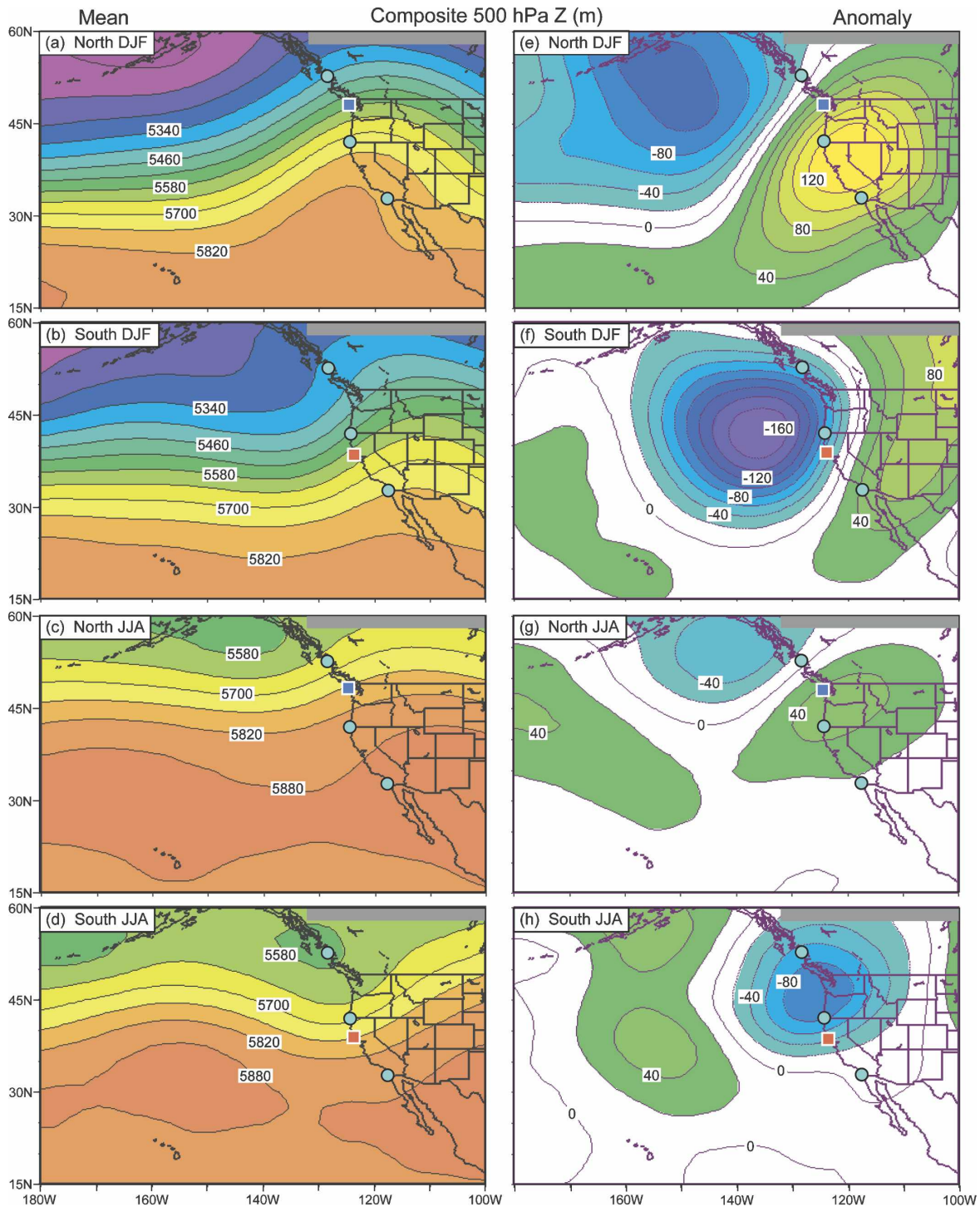


FIG. 6. Same as in Fig. 5, but for 500-hPa geopotential height ( $Z$ , m).

time relative humidity profiles are significantly drier (Fig. 10d) due to their warmth. The summer profiles are accompanied by much weaker flow (i.e., weaker storm systems) than during winter (Fig. 10e). Overall, then, IVT in atmospheric rivers reaching the coast is weaker

in summer than winter (e.g., Figs. 5a–d). The wind direction profiles (Fig. 10f) display an equally significant distinction between winter and summer. During winter for both north and south coasts, the profiles veer strongly with height from southerly at the surface to

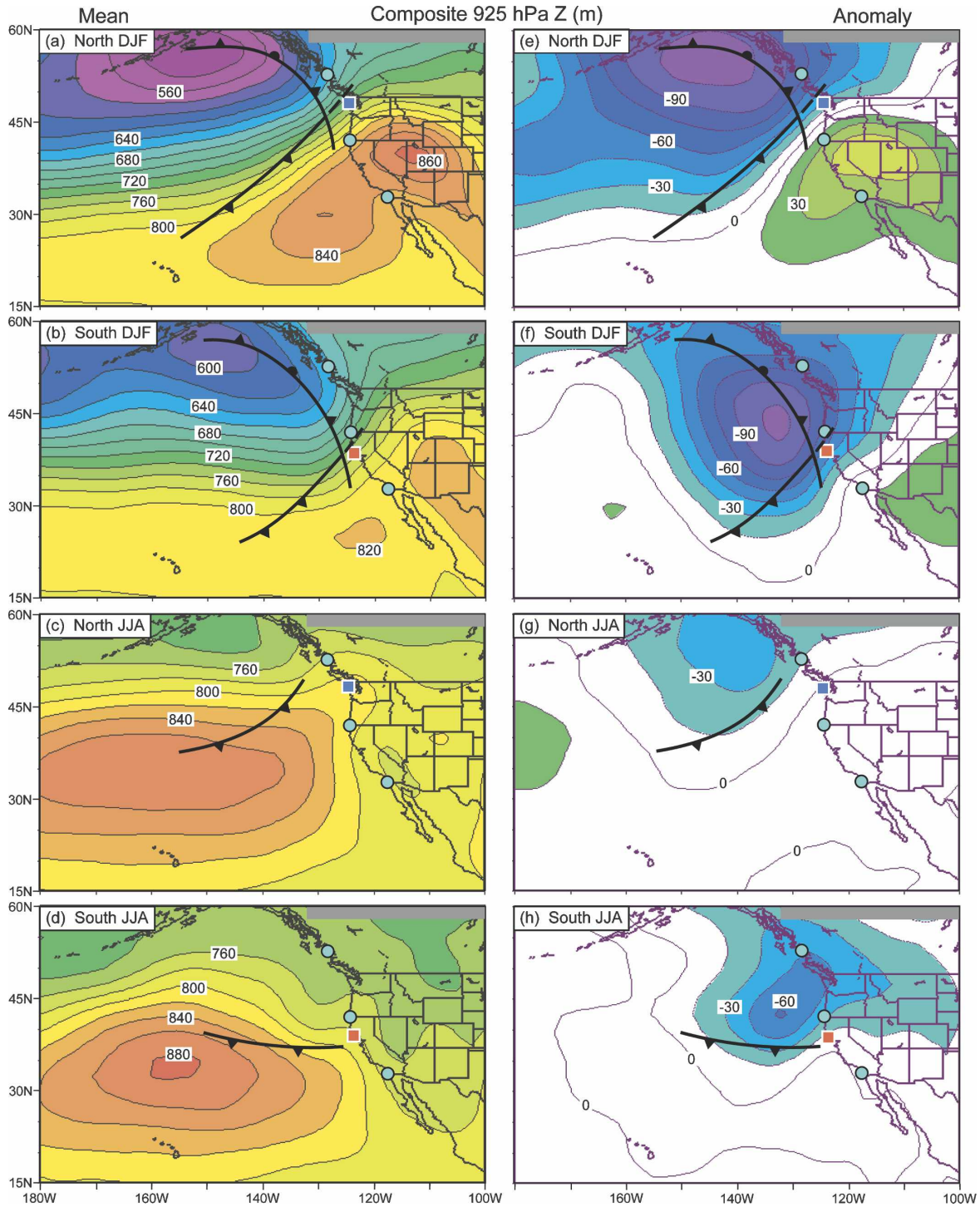


FIG. 7. Same as in Fig. 5, but for 925-hPa geopotential height ( $Z$ , m).

southwesterly at 3 km, indicating warm advection in the pre-cold-frontal environment. In contrast, the summer profiles portray directional backing with height in the lowest 2–3 km, from west-southwesterly to southwesterly at the north coast and from west-northwesterly to

west-southwesterly at the south coast. This vertically backing flow regime is a manifestation of the quasi-permanent anticyclone over the Pacific during summer. Consequently, the vapor transport directed orthogonal to the coastal topography (i.e., directed from 230° at

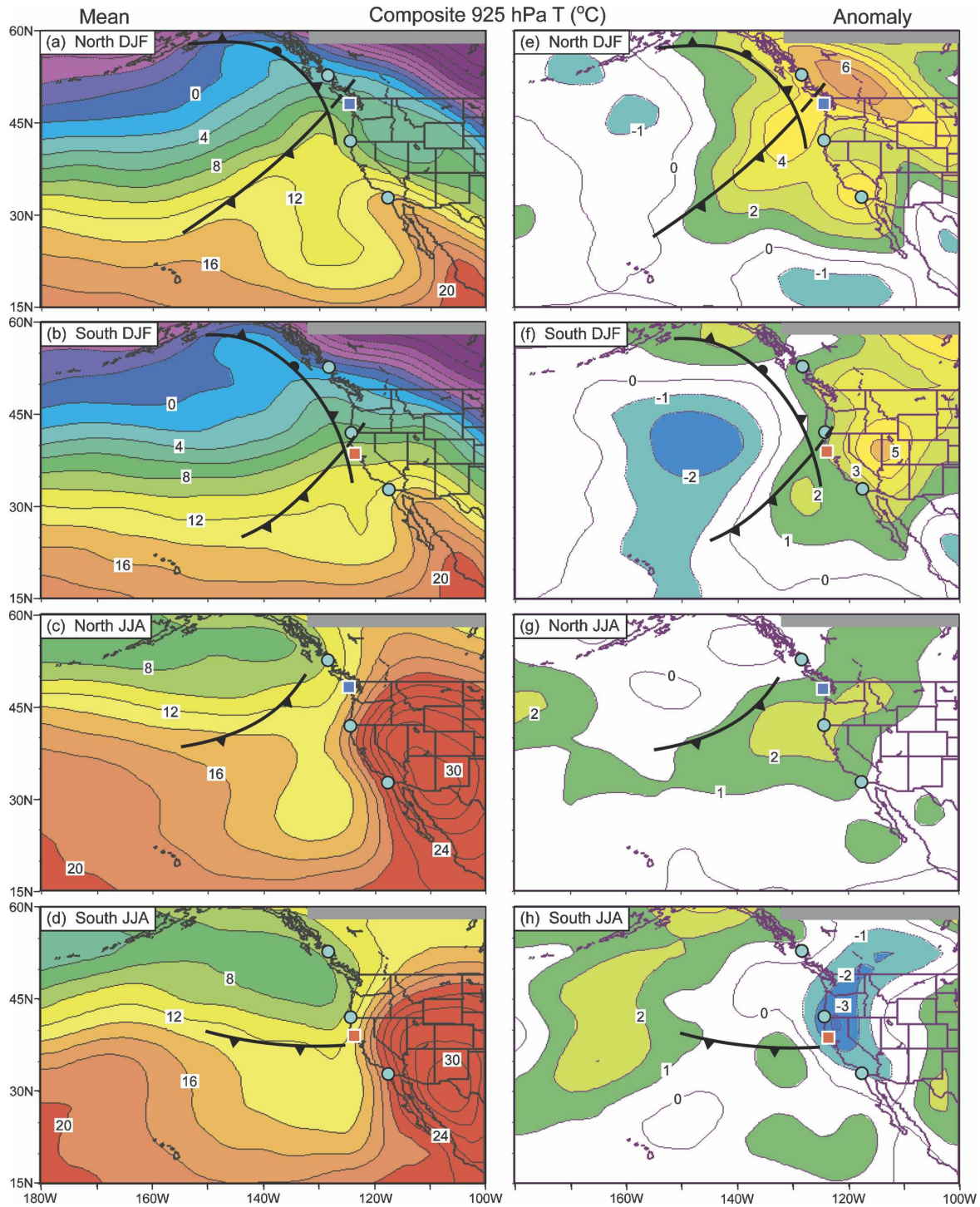


FIG. 8. Same as in Fig. 5, but for 925-hPa temperature ( $T$ ,  $^{\circ}\text{C}$ ).

both sites; Fig. 10g) is several-fold greater in the lowest 3 km during winter than summer, despite the fact that the water vapor content is greater in summer. This seasonal difference in terrain-normal vapor transport, together with the fact that the winter profiles are more

nearly saturated over a deeper layer than in summer, establishes the conditions under which landfalling atmospheric rivers are far more likely to yield orographically enhanced precipitation along the mountainous west coast of North America in winter than summer (as

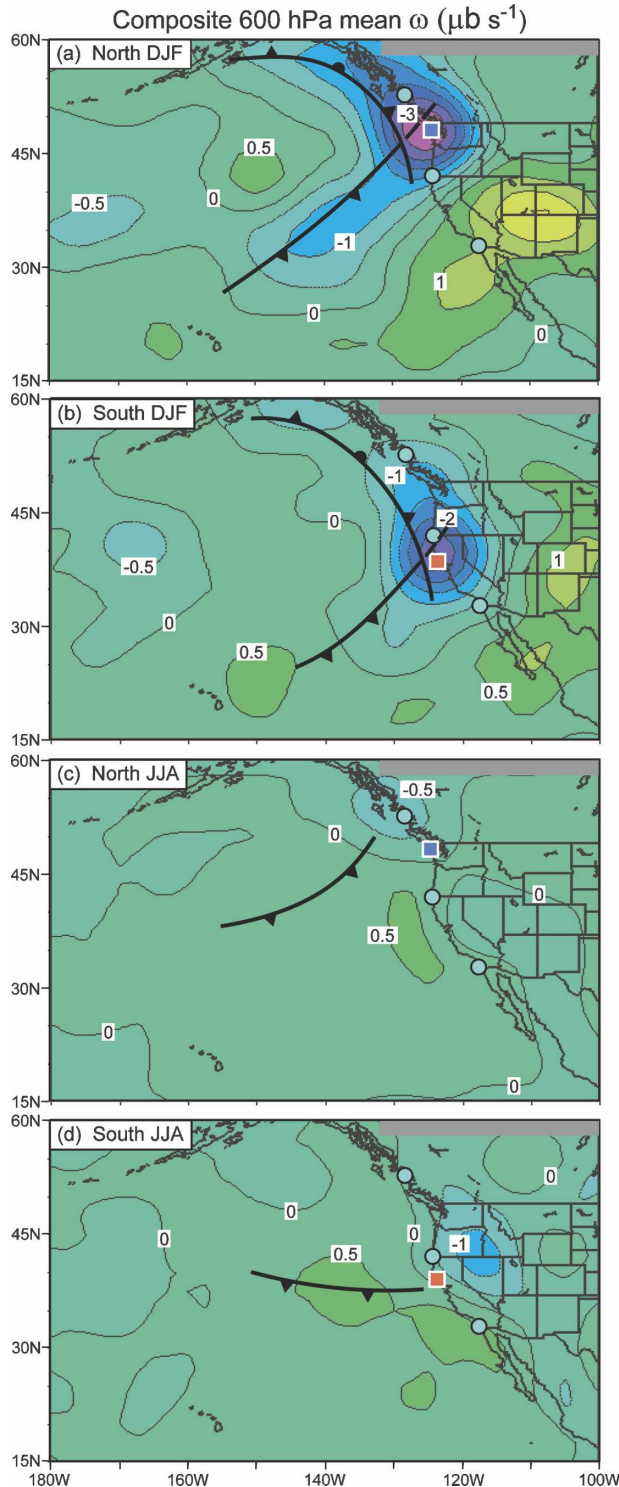


FIG. 9. Same as in Figs. 5a–d, but for 600-hPa vertical velocity ( $\omega$ ;  $\mu\text{b s}^{-1}$ ).

confirmed by the precipitation observations in Fig. 4). Finally, composite profiles of vertical velocity show strong ascent at both sites only during the winter (Fig. 10h), in keeping with Fig. 9, and reflect the fact that landfalling atmospheric rivers during winter are associated with stronger storms that produce more synoptic-scale precipitation than during summer.

## 2) OVERLAND HYDROCLIMATIC IMPACTS

The geographic and seasonal variability of precipitation tied to atmospheric rivers is explored further by examining direct precipitation and snowpack observations in the north-coast and south-coast domains (i.e., in Washington–Oregon and in California, respectively). Figure 11 presents the daily range of change in snow water equivalent ( $\Delta\text{SWE}$ ) at 128 snow pillow sites in Washington–Oregon and 119 snow pillow sites in California for all days and for atmospheric-river days during WY1998–2005. In both the north-coast and south-coast regions, atmospheric rivers predominantly increase SWE in the autumn and winter and decrease SWE in the spring. During the summer months, snow cover is generally absent, and no snow accumulates.

To place these  $\Delta\text{SWE}$  variations into perspective, the normalized fractions of precipitation and  $\Delta\text{SWE}$  for atmospheric-river days were calculated from each rain gauge and snow pillow site in the three West Coast states<sup>2</sup> as follows. First, season-averaged precipitation intensities were calculated as the sum of daily precipitation occurring at a station during the eight winters (summers) divided by the numbers of days with precipitation during those winters (summers). Then, the normalized precipitation fraction from days with atmospheric rivers was calculated as the average precipitation intensity on atmospheric-river days divided by the average precipitation intensity on all days. Values greater (less) than one signify that atmospheric-river storms produced more (less) precipitation than all storms. Normalized  $\Delta\text{SWE}$  fractions associated with atmospheric-river days were calculated in the same way. Because of the geographic diversity of the mountains in Washington and Oregon, those data were segregated into three regions: the Coast Ranges (8 sites), Cascades (90 sites), and inland ranges (30 sites).

Normalized fractions of precipitation and  $\Delta\text{SWE}$  for atmospheric-river days are shown in Fig. 12. The normalized precipitation fractions during winter in the north- and south-coast domains (Figs. 12a,d) show that,

<sup>2</sup> All of the rain gauges we used in Washington and Oregon are collocated with the snow pillows, but this is not the case in California. A total of 407 California rain gauges were used.

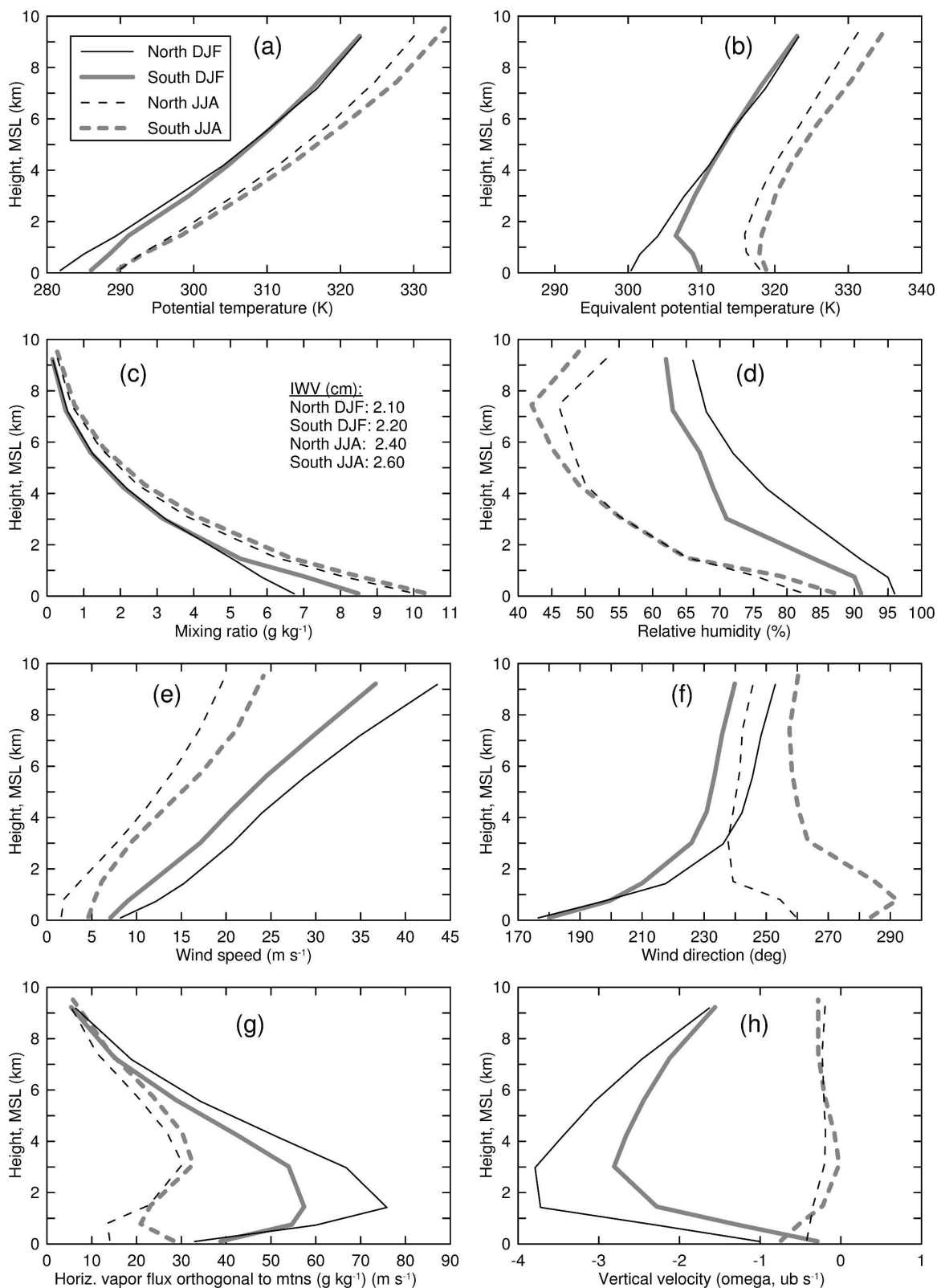


FIG. 10. Composite NCEP-NCAR daily reanalysis profiles at Cape Flattery, WA (north-coast; black), and Bodega Bay, CA (south-coast; gray shaded), for SSM/I IWV plumes intersecting the north-coast and south-coast domains, respectively, in winter (solid) and summer (dashed): (a) potential temperature (K), (b) equivalent potential temperature (K), (c) water vapor mixing ratio ( $\text{g kg}^{-1}$ ), (d) relative humidity (%), (e) wind speed ( $\text{m s}^{-1}$ ), (f) wind direction ( $^{\circ}$ ), (g) horizontal water vapor flux ( $\text{g kg}^{-1}(\text{m s}^{-1})$ ) directed orthogonal to the local mountains (i.e., from  $230^{\circ}$ ), and (h) vertical velocity ( $\omega$ ;  $\mu\text{b s}^{-1}$ ).

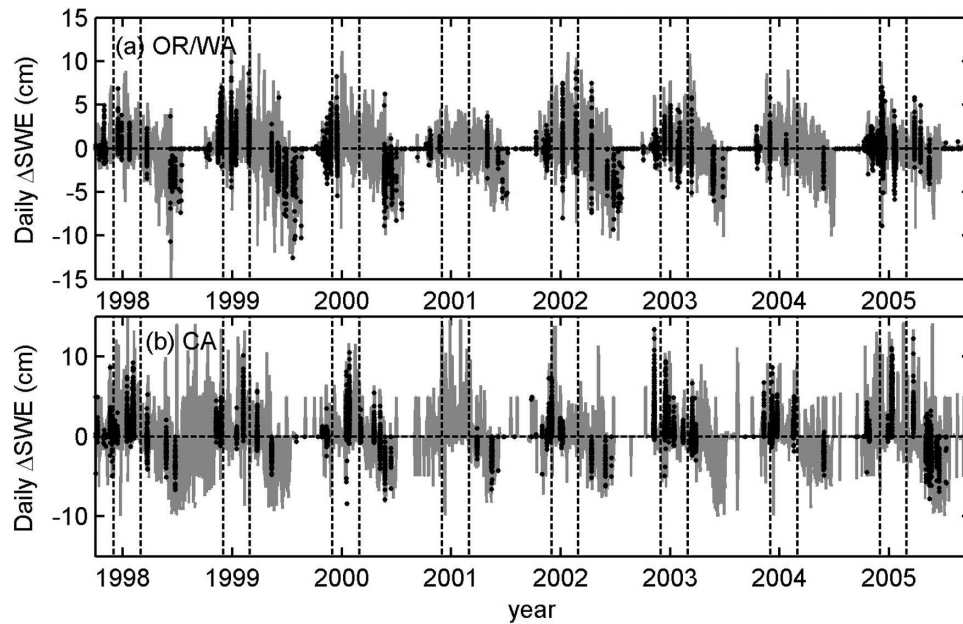


FIG. 11. Daily range of change in snow water equivalent at individual stations [ $\Delta$ SWE (cm)]—depicted as gray-shaded lines] during the water years 1998–2005 at snow pillow sites in (a) Washington–Oregon and (b) California. The black dots in (a) and (b) denote daily  $\Delta$ SWE at individual stations on those days when IWV plumes intersected the north-coast and south-coast domains, respectively. The pairs of vertical dashed lines bound the DJF time windows.

on average, roughly twice as much precipitation as normal falls during atmospheric-river storms. In addition, among the north-coast stations (Fig. 12a), the coastal ranges receive a greater precipitation enhancement during atmospheric-river conditions, then the Cascades, followed by the inland ranges. This behavior can be explained partly by the proximity of these ranges to the oceanic source region of the atmospheric rivers, and also because each successive mountain range scavenges moisture via orographic precipitation processes [as was depicted analytically in Schneidereit and Schär (2000) for flows over the southern European Alps].

During summer, atmospheric rivers, on average, do not yield significant precipitation enhancements (Figs. 12b,e). It is plausible that most of the summer rains on the West Coast are convective in character, perhaps becoming enhanced on occasion by deep moisture originating from the Mexican summer monsoon. In contrast, the summertime atmospheric rivers detected in the SSM/I imagery originated over the cool North Pacific, where the overlying moisture content is comparatively small. That, coupled with the fact that the lower-tropospheric flow and terrain-normal moisture transport in atmospheric rivers are weak during the summer (Figs. 10e–g), conspires to make them only modest precipitation producers, especially when gauged against their much wetter winter counterparts.

The normalized  $\Delta$ SWE fractions in the south-coast

domain during winter (Fig. 12f) nearly all are greater than unity and show, on average, roughly twice the normal gain during atmospheric-river storms—consistent with the mean value of 2 for the companion normalized precipitation fraction (Fig. 12d). In contrast, the north-coast  $\Delta$ SWEs during atmospheric-river conditions are, on average, similar to all storms (i.e., the mean normalized  $\Delta$ SWE fraction =  $\sim 1$ ; Fig. 12c), despite the fact that these atmospheric-river storms generate copious precipitation (Fig. 12a). In addition, the lowest-elevation sites in Washington and Oregon gain consistently less snow than normal with atmospheric-river events, and some of these sites actually lose snow. The normalized  $\Delta$ SWE and precipitation characteristics observed at the comparatively low-elevation north-coast sites arise because landfalling wintertime atmospheric rivers tend to be accompanied by anomalously warm conditions (e.g., Fig. 8) that often yield rain rather than snow at low elevations, resulting in rain-on-snow melting of standing snowpacks. In short, atmospheric rivers contribute more to the snowpack of California’s high Sierra Nevada than they do to the lower mountain ranges of the Pacific Northwest.

#### b. Wintertime variability based on IWV content

Because wintertime atmospheric rivers generate much more precipitation than their summertime coun-

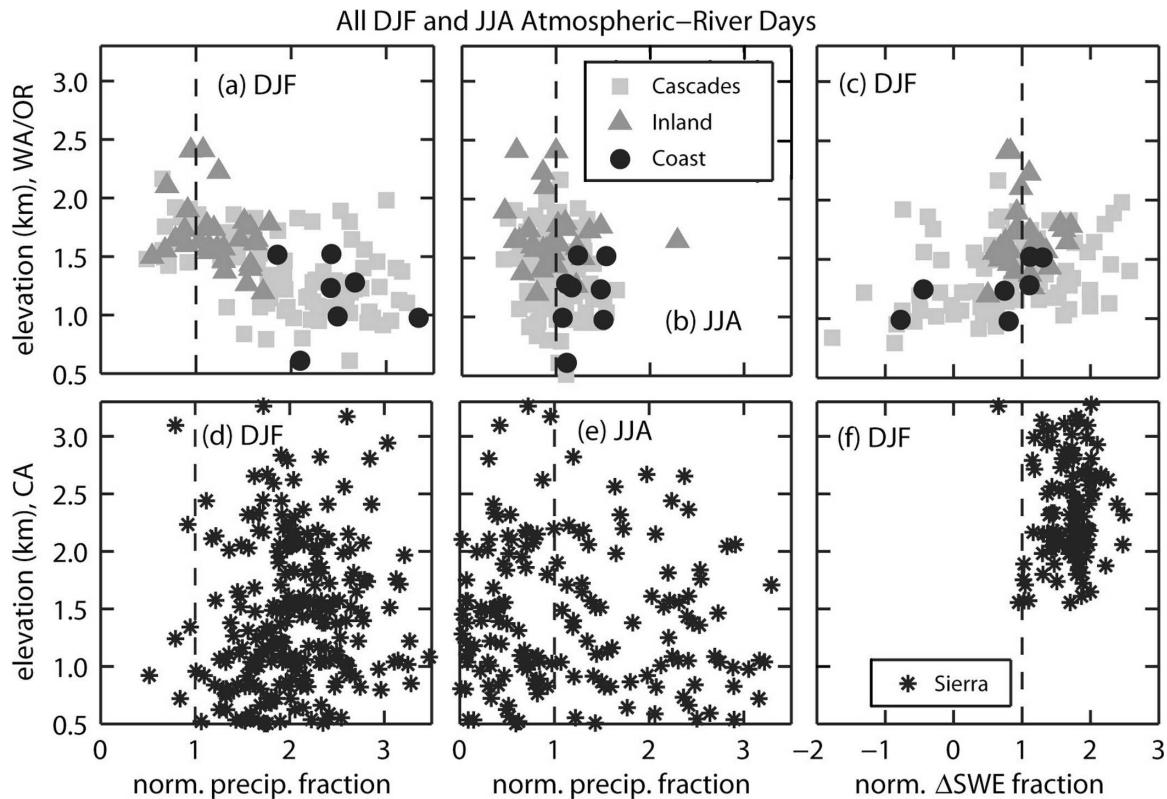


FIG. 12. (a)–(c) Precipitation and snow observations at sites in Washington–Oregon for water years 1998–2005 when SSM/I IWV plumes intersected the north coast: normalized precipitation fraction for atmospheric river days during (a) winter and (b) summer, and (c) normalized  $\Delta$ SWE fraction for atmospheric river days during winter. (d)–(f) Same as in (a)–(c), except the observations are for California when SSM/I IWV plumes intersected the south coast. The sites in Washington–Oregon are segregated by region: black circles = Coast Ranges, light-gray squares = Cascades, and medium-gray triangles = inland ranges (east of the Cascades). The 1:1 ratio is marked with a vertical dashed line in each panel.

terparts (Figs. 4, 12), they quite likely yield greater overall societal impacts across western North America. Hence, this subsection explores the sensitivity of the synoptic characteristics of atmospheric rivers to the SSM/I IWV content within these rivers for winter events only. Wintertime IWV plumes with the greatest water vapor content (i.e., those with coherent regions of IWV  $>3$  cm within 1000 km of the coast) are identified in Tables 1 and 2, and they number 11 out of a total of 29 (37.9%) for the north coast and 15 of 35 (42.9%) for the south coast. Composites based on all of the days with wintertime IWV plumes (i.e., those with core values  $>2$  cm, which include those with core values  $>3$  cm) are hereafter referred to as the “standard” or “all” cases. The subset of winter days with core IWV values only surpassing 3 cm will be described as “strong.” Fig. 1 shows an example of a strong plume.

Composites of reanalysis IWV fields based on all IWV-plume days and on the strong days in the north- and south-coast domains are shown in Fig. 13. As expected, the composite IWV plumes during the strong

cases contain more water vapor than during the standard cases. The synoptic-frontal context is essentially identical for the four composites. Reanalysis rainfall at the coast and along the cold front offshore is greater for the strong composites (Fig. 14), consistent with observations from SSM/I and the NWS COOP network (not shown). Companion 600-hPa vertical velocity fields (not shown) exhibit corresponding differences in the distribution and magnitude of ascent between the standard and strong composites.

The reanalysis IVT composite mean fields (Fig. 15) display significantly greater water vapor transport in the north- and south-coast atmospheric rivers for the strong cases. The fact that the strong cases with large IVT yield more precipitation is consistent with an earlier finding by Pandey et al. (1999) of a direct relationship between the magnitude of lower-tropospheric moisture flux measured by soundings at Oakland, California, and the amount of precipitation falling in the Sierra Nevada. More recently, Junker et al. (2008) showed a similar linkage using global reanalysis data.

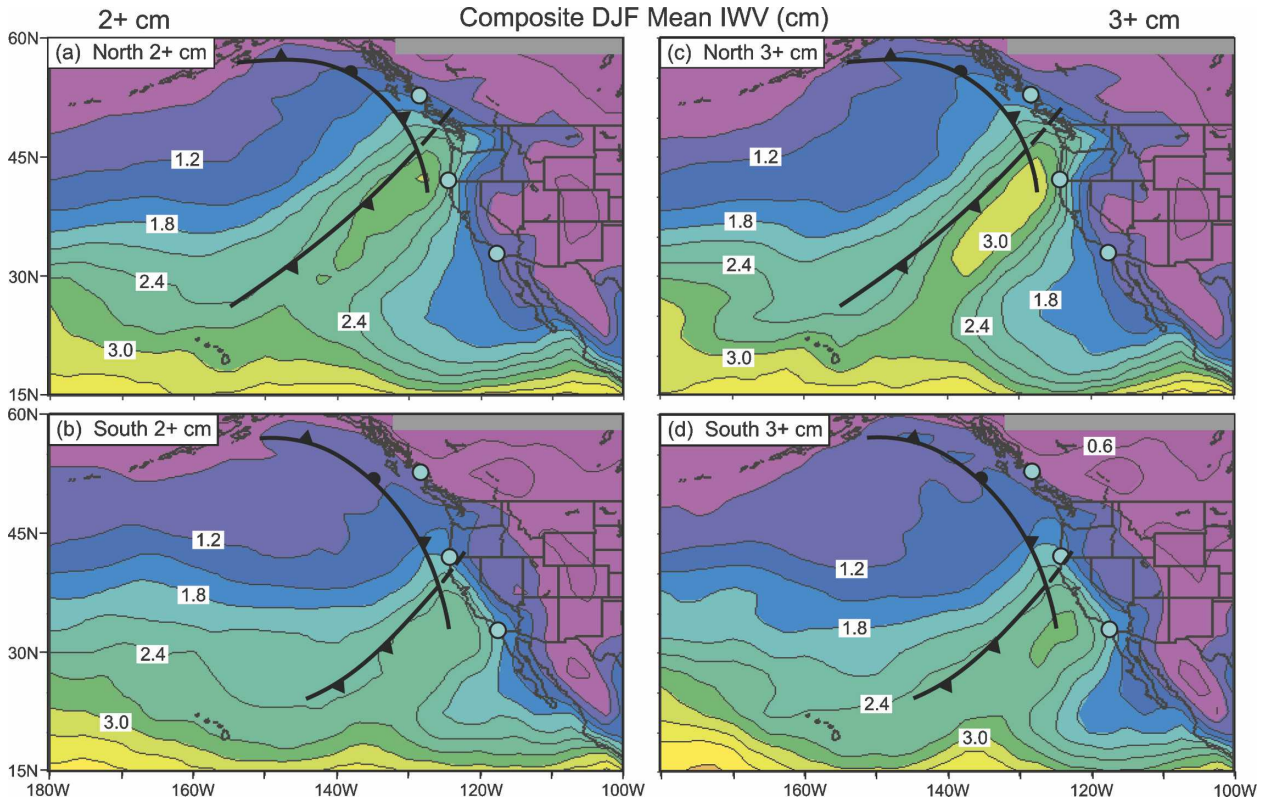


FIG. 13. Composite mean IWV (cm; same color scale as in Figs. 3e–h) derived from the NCEP–NCAR daily reanalysis dataset for wintertime SSM/I IWV plumes intersecting the north-coast and south-coast domains on a daily basis (0000–0000 UTC), stratified by the minimum core value of IWV within these plumes: (a) north, >2 cm, (b) south, >2 cm, (c) north, >3 cm, and (d) south, >3 cm. The bold light-blue dots and fronts are as in Fig. 3.

The larger IVT in the strong cases is a reflection, in part, of the greater IWV content. Inspection of the corresponding 925-hPa geopotential height anomaly composites (Fig. 16) provides additional insight into the larger IVT for the strong cases. Specifically, the strong cases are associated with much larger negative height anomalies (i.e., stronger storms) over the eastern Pacific than their standard counterparts, whereas the magnitude of ridging over western North America is little changed between the strong and standard composites. Consequently, stronger flow is directed toward the coast in the vicinity of the landfalling plumes, on average, during the strong cases (as is also revealed in 925-hPa mean wind speed composites; not shown). Geopotential height anomalies and mean wind speed composites above 925 hPa (not shown) exhibit comparable differences between the standard and strong cases. Consequently, the increase in the magnitude of IVT between the standard and strong cases arises due to greater IWV content *and* stronger winds in the strong cases. Interestingly, the 925-hPa temperature anomalies (not shown) show little difference in magnitude between the standard and strong cases. Because the

strong cases contain roughly the same sensible heat content but more IWV than the standard cases, the stronger cases are more nearly saturated (as is revealed in relative humidity composites; not shown). This, together with the fact that the strong cases exhibit stronger flow directed toward the coast, contributes to greater orographic precipitation along the coast, as implied in Fig. 14 and verified with the SSM/I and COOP rainfall observations.

The results described in this subsection partly explain the frequency of flooding that was observed on the Russian River in northern California between 1 October 1997 and 28 February 2006 (Fig. 1; Ralph et al. 2006). Namely, of the five Russian River floods reported during the WY1998–2005 period studied here, all five corresponded to wintertime atmospheric rivers crossing the south coast and four of those occurred when strong IWV plumes made landfall (Table 2). The two remaining floods occurred during WY2006, and both were tied to the landfall of south-coast wintertime atmospheric rivers with strong IWV plumes. Thus, although the total number of IWV plumes (i.e., atmospheric rivers) along the south coast was considerably

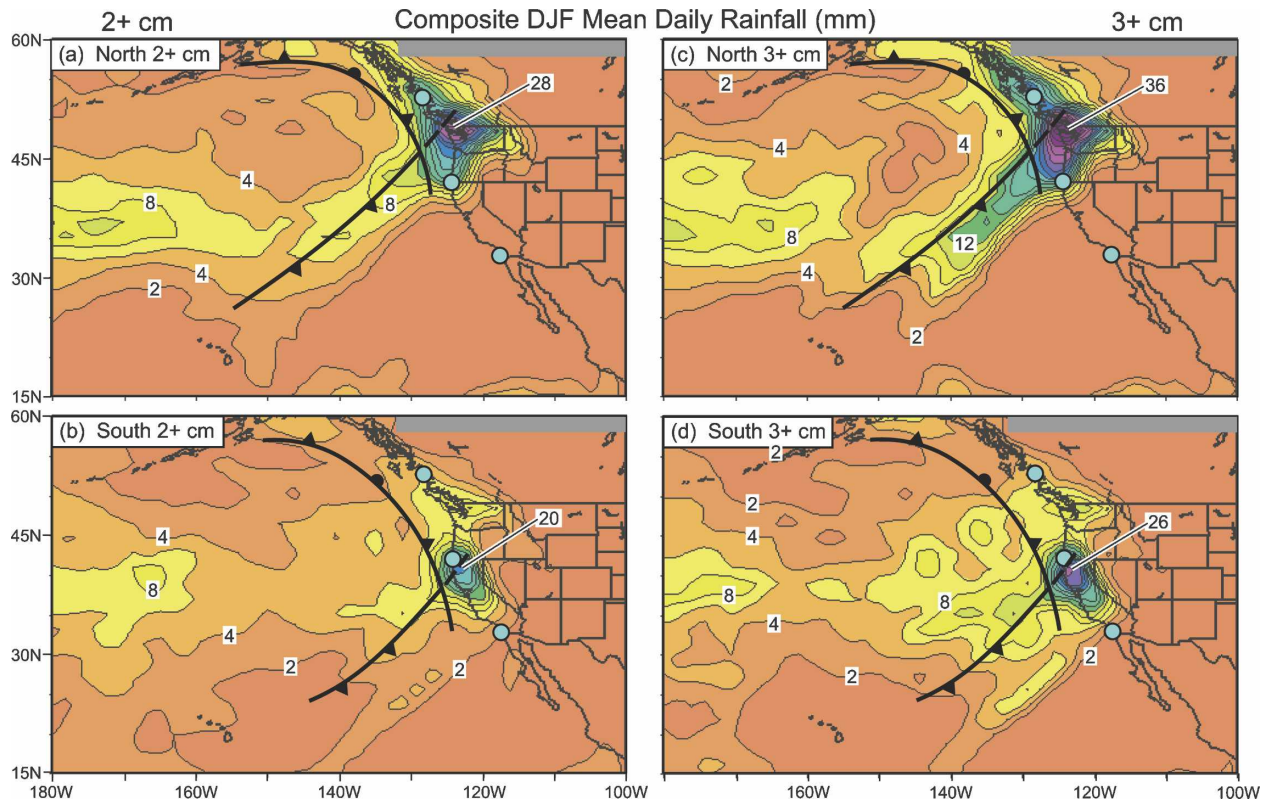


FIG. 14. Same as in Fig. 13, but for daily rainfall (mm).

greater than the number of floods (126 plumes versus 7 floods), IWV plumes only contributed to flooding when they made landfall during winter, especially if they contained enhanced water vapor content. This result is consistent with the fact that coastal precipitation exhibits the greatest enhancement during the landfall of strong wintertime IWV plumes (Fig. 14).

## 6. Conclusions

Atmospheric rivers are an important and, until recently, a largely unappreciated component of the atmospheric arm of the global water cycle. This paper has demonstrated that, when atmospheric rivers make landfall over western North America (from the California–Mexico border northward into British Columbia), they significantly modify the climate and yield important storms and hydrologic consequences. Polar-orbiting satellite imagery was used here as a baseline for detecting landfalling atmospheric rivers that extended from over the eastern Pacific to the west coast of North America between 1997 and 2005. Using the dates of atmospheric-river episodes detected thus, composite synoptic analyses and detailed precipitation analyses of

the meteorological conditions associated with the rivers were developed. These composites provided the basis for the first long-term regional characterization of the conditions and impacts associated with atmospheric rivers, with findings summarized as follows.

Twice-daily SSM/I satellite-image composites of IWV were used to detect landfalling atmospheric rivers along adjacent north- and south-coast regions of western North America during eight water years. Long (>2000 km) and narrow (<1000 km) plumes of enhanced IWV exceeding 2 cm were a strong indicator of atmospheric rivers. Those plumes making landfall in Oregon, Washington, and British Columbia for a full calendar day were included in the inventory of north-coast atmospheric-river landfalls, while those plumes making landfall in California were grouped into the inventory of south-coast landfalls. The north coast experienced 301 days with atmospheric rivers, while the south coast only 115. Most atmospheric rivers occurred during the warm season in the north and cool season in the south, despite the fact that the cool season is climatologically wettest for both regions. An additional tier of stratification was performed for the diametrically opposed winter and summer seasons. Composite daily SSM/I IWV analyses show landfalling wintertime atmo-

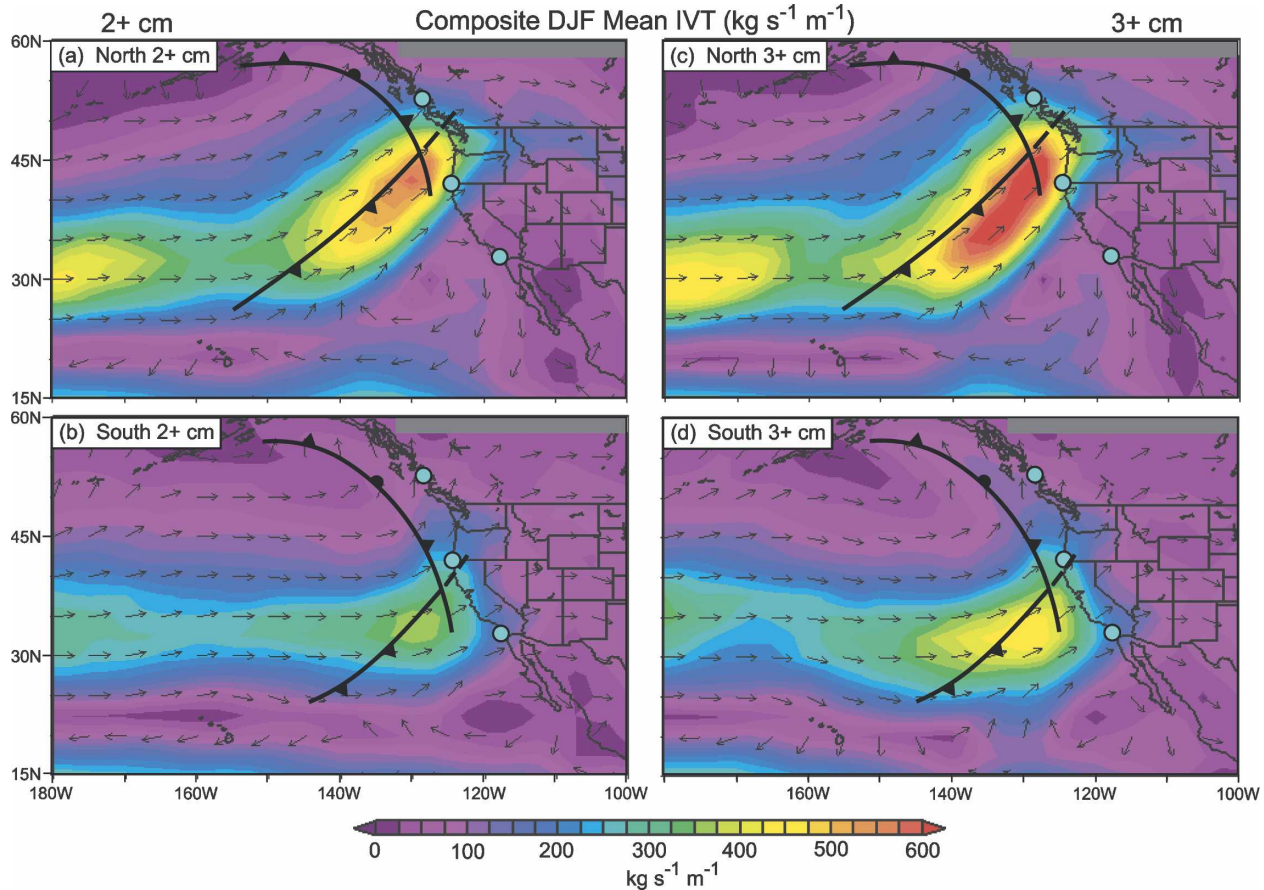


FIG. 15. Same as in Fig. 13, but for IVT ( $\text{kg s}^{-1} \text{m}^{-1}$ ). Vectors are as in Fig. 5.

spheric rivers extending northeastward from the tropical eastern Pacific, whereas the summertime composite rivers were zonally oriented and, thus, did not originate directly from the tropics. Companion SSM/I composites of daily rainfall show large orographic enhancement during the landfall of winter (but not summer) atmospheric rivers.

Composites of NCEP–NCAR global, daily reanalysis fields accurately identified the position and orientation of the composite IWV plumes and precipitation distributions retrieved from the SSM/I. The atmospheric rivers associated with these features produced anomalous warmth, a trough offshore, and ridging over the Intermountain West in the winter and north-coast summer reanalysis composites, whereas the south-coast summer atmospheric-river composite coincided with relatively cool conditions and a trough near the coast. The greatest contrasts in atmospheric-river characteristics were seasonally dependent, as is highlighted in a multipanel conceptual diagram (Fig. 17). Specifically, atmospheric rivers were accompanied by strong IVT impinging on the West Coast in the pre-cold-frontal environment in

winter, while there were weak IVTs in post-cold-frontal conditions in summer. Even though the IWV in atmospheric rivers was greater in summer, the vapor fluxes were stronger in winter due to much stronger flows associated with more intense storms. In addition, the wintertime rivers showed a substantial meridional vapor transport component extending from the tropics to the coast, whereas the summertime counterparts were roughly zonally aligned. This seasonal difference highlights the fact that vapor transports in the wintertime rivers were oriented more nearly orthogonal to the mountain ranges—a scenario that favors orographic precipitation enhancement. Thus, atmospheric rivers had far greater impacts on precipitation production onshore in winter than summer, because the terrain-normal vapor fluxes and synoptic upward motions were both stronger in winter, during which the air was more nearly saturated (not shown in Fig. 17). Consequently, the wintertime atmospheric rivers quite likely incurred more substantial societal impacts in westernmost North America. During winter, atmospheric rivers with the largest IWV were associated with more intense storms

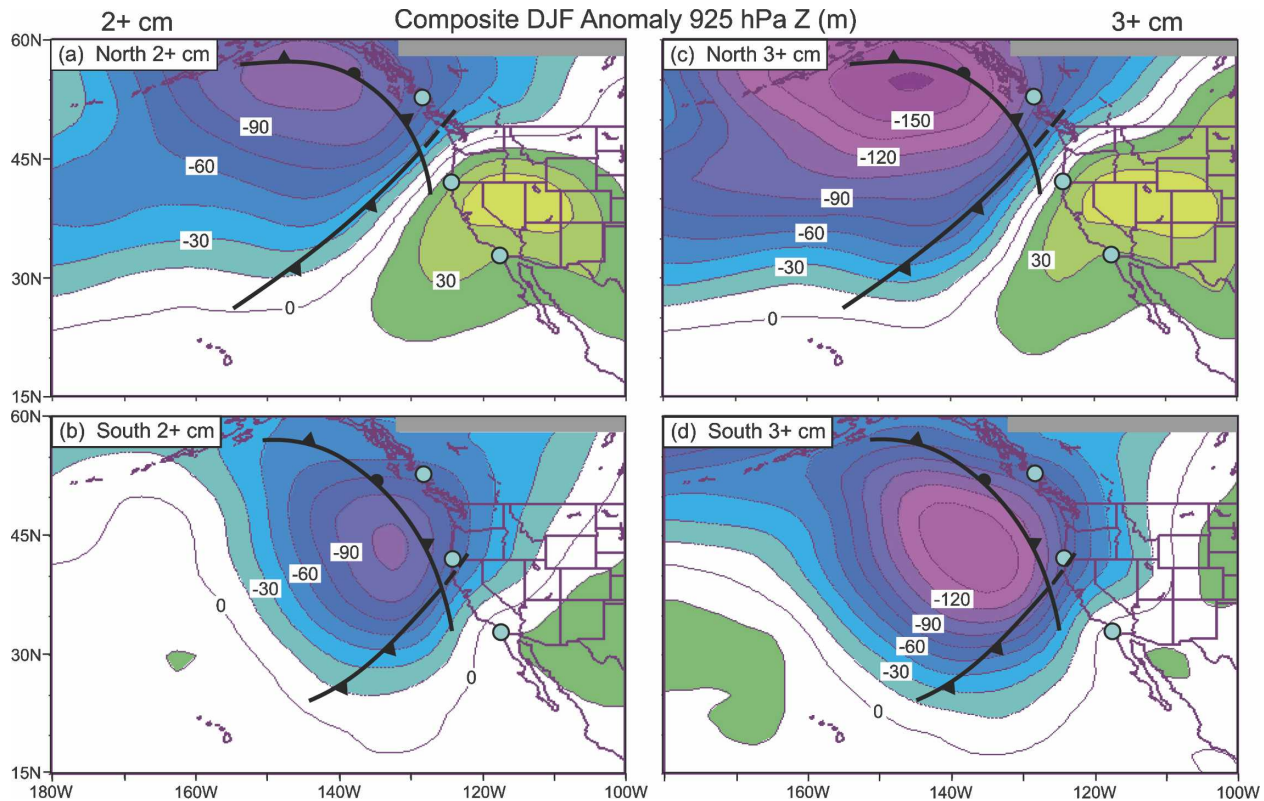


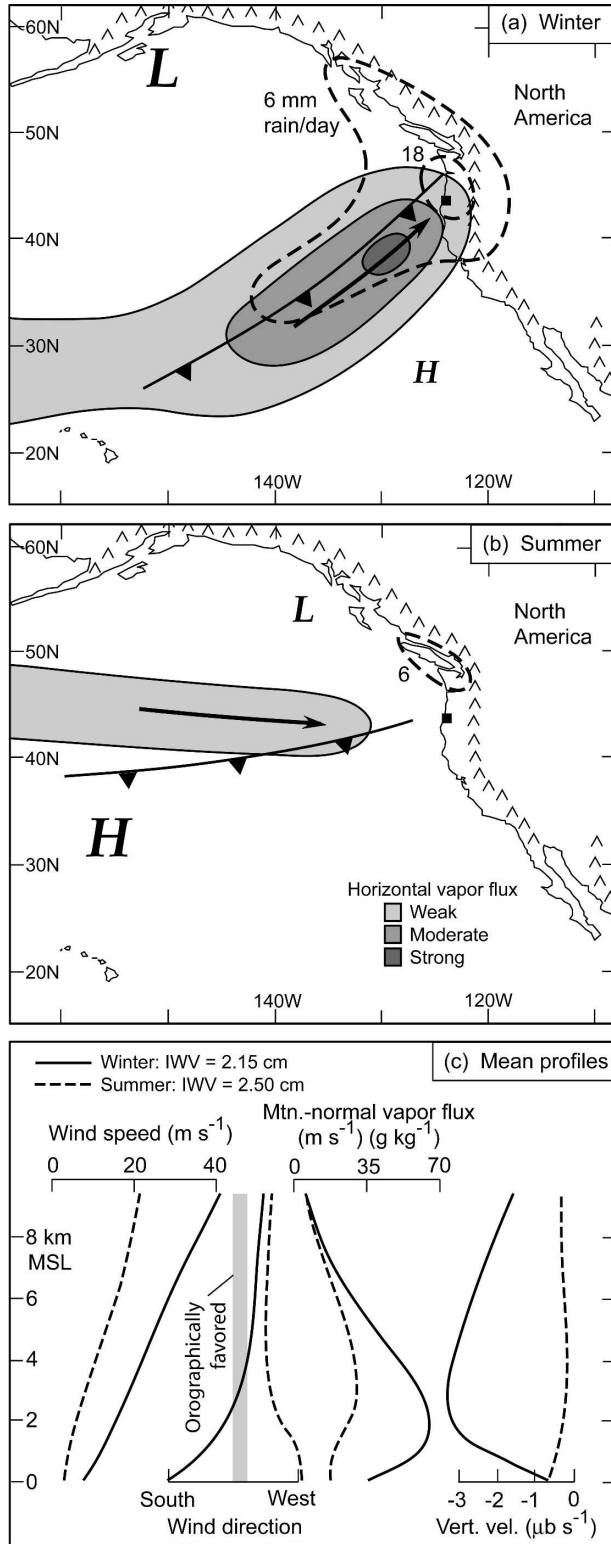
FIG. 16. Same as in Fig. 13, but for 925-hPa geopotential height anomalies ( $Z$ , m).

with stronger flows and vapor fluxes, and more precipitation (not shown in Fig. 17).

The relatively broad ( $\sim 2000$  km) width scale of the atmospheric rivers represented in the NCEP–NCAR reanalysis IWV and IVT composites is considerably larger than the narrow ( $< 1000$  km wide) SSM/I IWV plumes on which these reanalysis composites were based. These atmospheric-river composites are also much broader than the  $\sim 400$ -km-wide plume of enhanced IWV and IVT measured by a curtain of National Oceanic and Atmospheric Administration (NOAA) P-3 dropsondes across an atmospheric river offshore of California (Ralph et al. 2004) and a similarly narrow atmospheric river that produced record flooding in northern California (Fig. 1; Ralph et al. 2006). The artificial broadening of the atmospheric-river composites can be attributed primarily to the compositing of narrow atmospheric rivers with differing positions and orientations. Although not obvious in the composites, the coarse ( $\sim 250$  km) horizontal resolution of the reanalysis dataset also ensures that the reanalysis IVT plumes on individual days are much broader (e.g., Figs. 1 and 2 in Dettinger 2004) than the atmospheric rivers revealed by more highly resolved data sources such as SSM/I and dropsondes. Despite the artificial broaden-

ing, the reanalysis composites have confirmed that the IWV plumes evident in the SSM/I data correspond to regions of strong horizontal water vapor transport. These composites also provide considerable insight into the geographically and seasonally modulated synoptic characteristics and overland impacts of landfalling atmospheric rivers, with the acknowledgment that the width scale of individual atmospheric rivers is much narrower than the north- or south-coast domains used in this study.

Regional precipitation and snowpack networks were used to further explore the overland impacts of landfalling atmospheric rivers. On average, roughly twice the normal precipitation fell when winter storms exhibited atmospheric-river attributes, whereas near-normal precipitation fell during the climatologically drier summertime storms when atmospheric-river conditions were present. During winter in the north-coast domain, the coastal ranges received the greatest boost in precipitation during atmospheric-river storms, followed by the Cascades, and then the inland ranges. This behavior can be explained partly by the proximity of these ranges to the oceanic source region of the atmospheric rivers, and also because each successive mountain range scavenged moisture via orographic precipitation processes.



The winter precipitation enhancement in the south-coast domain (i.e., in California's high Sierra Nevada) was much more uniform from site to site.

Regarding snowpack, atmospheric rivers most often increased SWE in autumn/winter and decreased SWE in spring. On average, wintertime SWE in the south-coast domain exhibited twice the normal gains during atmospheric-river storms. In contrast, the average increase in SWE in the somewhat lower north-coast mountains was not significantly modulated by atmospheric rivers, despite the fact that these atmospheric rivers produced copious precipitation (like their southern counterparts). In fact, the lowest-elevation sites in the north consistently gained less snow than normal with atmospheric-river events, and some of these sites actually lost snow. This situation arose because land-falling wintertime atmospheric rivers tend to be accompanied by anomalously warm conditions that often yield rain rather than snow at lower elevations, resulting in rain-on-snow melting of standing snowpacks—which increases the likelihood of flooding. In short, atmospheric rivers contributed more to the snowpack in the higher terrain. The combination of anomalies and enhancements associated with landfalling atmospheric rivers ensures that they provide important inputs to the water resources and landscapes of the West. Storms from the most powerful atmospheric rivers also can produce floods and debris flows, so that their occurrences are often mixed blessings. Because atmospheric rivers contribute significantly to precipitation, snowpack modulation, and flooding in western North America, they represent a key phenomenon linking weather and climate.

FIG. 17. Conceptual representation of synoptic conditions associated with landfalling atmospheric rivers during summer and winter, based on an average of the north-coast and south-coast reanalysis composites. (a) Wintertime mean plan view of IVT (solid contours; light shading: weak water vapor flux of  $250\text{--}350 \text{ kg s}^{-1} \text{ m}^{-1}$ , medium shading: moderate flux of  $350\text{--}450 \text{ kg s}^{-1} \text{ m}^{-1}$ , dark shading: strong flux  $>450 \text{ kg s}^{-1} \text{ m}^{-1}$ ), daily rainfall (dashed;  $\text{mm day}^{-1}$ ), 925-hPa cold front (standard notation) and pre-cold-frontal flow direction (bold arrow), and the location of the primary cyclone and anticyclone (L and H, respectively; the size of the letters reflect their relative intensities). The black square marks the position of the composite sounding shown in (c). The primary near-coast mountains are also shown. (b) Same as in (a), but for summertime conditions. (c) Mean profiles of wind speed and direction, mountain-normal water vapor flux, and vertical velocity for winter and summer (solid and dashed, respectively). The vertical gray-shaded bar in (c) marks the mean orientation orthogonal to the mountain ranges in the north-coast and south-coast domains (i.e., the orographically most favored flow direction).

The practical importance of atmospheric rivers is clearly evident from the present study, which has characterized the role of these foundational features of the atmospheric water cycle as expressed across the eastern North Pacific and westernmost North America. The analyses presented here extend a decade's worth of scientific observations and analyses in the region, and are aimed at consolidating our understanding of atmospheric rivers and their onshore effects. This kind of understanding, in turn, may provide the basis for improved predictability of both the atmospheric features and their onshore impacts. Improved understanding of atmospheric rivers, and how they are represented by SSM/I IWV data offshore, can factor significantly into the forecast process and can aid in the development of operational decision-support tools for quantitative precipitation forecasting and flood warnings along the U.S. West Coast (e.g., Morss and Ralph 2007). However, maintenance of these observations and analyses is not yet ensured in the long term, and plans for continuing observations need to be developed and implemented, now that we know their importance. At the same time, because the benefits and threats posed by landfalling atmospheric rivers tend to appear in (relatively) infrequent extreme events, additional analyses—drawing on longer historical records—are needed in order to understand the more infrequent and extreme outcomes of the landfalls. Consequently, we have embarked on follow-on studies to gauge the overland hydrologic impacts of these extreme events based on their detection throughout the almost 60 yr of NCEP–NCAR global reanalysis data. We are also in the process of assessing the important dynamical and topographically modulated distinctions between atmospheric-river storms and their non-atmospheric-river counterparts using regional-scale reanalysis datasets.

*Acknowledgments.* We thank Cathy Smith of NOAA's Earth System Research Laboratory, and her colleagues at the former NOAA–CIRES Climate Diagnostics Center, for developing the NCEP–NCAR reanalysis composite tools and making them available at <http://www.cdc.noaa.gov>. These tools were an indispensable component of the research presented in this paper. Jim Adams electronically drafted the majority of the figures presented in this paper, and Allen White of NOAA/ERSL generously donated time to generate two additional figures. Support for Mike Dettinger's contributions was provided by the U.S. Geological Survey's Hydroclimate and San Francisco Bay Ecosystems Programs. We greatly appreciate the input from Dr. Jeff Whitaker of NOAA's Earth System Research Laboratory, and from three anonymous reviewers.

Their efforts improved the scope and quality of this paper.

#### REFERENCES

- Beaumont, R. T., 1965: Mt. Hood pressure pillow snow gage. *J. Appl. Meteor.*, **4**, 626–631.
- Bergeron, T., 1937: On the physics of fronts. *Bull. Amer. Meteor. Soc.*, **18**, 265–275.
- Browning, K. A., 1990: Organization of clouds and precipitation in extratropical cyclones. *Extratropical Cyclones: The Erik Palmén Memorial Volume*, C. W. Newton and E. Holopainen, Eds., Amer. Meteor. Soc., 129–153.
- , and C. W. Pardoe, 1973: Structure of low-level jet streams ahead of mid-latitude cold fronts. *Quart. J. Roy. Meteor. Soc.*, **99**, 619–638.
- Carlson, T. N., 1991: *Mid-Latitude Weather Systems*. HarperCollins, 507 pp.
- Dettinger, M. D., 2004: Fifty-two years of “pineapple-express” storms across the West Coast of North America. U.S. Geological Survey, Scripps Institution of Oceanography for the California Energy Commission, PIER Project Rep. CEC-500-2005-004, 20 pp. [Available online at <http://www.energy.ca.gov/2005publications/CEC-500-2005-004/CEC-500-2005-004.PDF>.]
- Farnes, P. E., 1967: Criteria for determining mountain snow pillow sites. *Proc. 35th Western Snow Conf.*, Boise, ID, Western Snow Conference, 59–62.
- Ferraro, R. R., S. J. Kusselson, and M. Colton, 1998: An introduction to passive microwave remote sensing and its application to meteorological analysis and forecasting. *Natl. Wea. Dig.*, **22**, 11–23.
- Ferriday, J. G., and S. K. Avery, 1994: Passive microwave remote sensing of rainfall with SSM/I: Algorithm development and implementation. *J. Appl. Meteor.*, **33**, 1587–1596.
- Goodberlet, M. A., C. T. Swift, and J. C. Wilkerson, 1990: Ocean surface wind speed measurements of the special sensor microwave/imager (SSM/I). *IEEE Trans. Geosci. Remote Sens.*, **28**, 823–828.
- Higgins, W., and Coauthors, 2006: The NAME 2004 field campaign and modeling strategy. *Bull. Amer. Meteor. Soc.*, **87**, 79–94.
- Hollinger, J. P., J. L. Peirce, and G. A. Poe, 1990: SSM/I instrument evaluation. *IEEE Trans. Geosci. Remote Sens.*, **28**, 781–790.
- Junker, N. W., R. H. Grumm, R. Hart, L. F. Bosart, K. M. Bell, and F. J. Pereira, 2008: Use of normalized anomaly fields to anticipate extreme rainfall in the mountains of northern California. *Wea. Forecasting*, in press.
- Kalnay, E., and Coauthors, 1996: The NCEP/NCAR 40-Year Reanalysis Project. *Bull. Amer. Meteor. Soc.*, **77**, 437–471.
- Katsaros, K. B., and R. M. Lewis, 1986: Mesoscale and synoptic-scale features of North Pacific weather systems observed with the Scanning Multichannel Microwave Radiometer on Nimbus-7. *J. Geophys. Res.*, **91**, 2321–2330.
- Lackmann, G. M., and J. R. Gyakum, 1999: Heavy cold-season precipitation in the northwestern United States: Synoptic climatology and an analysis of the flood of 17–18 January 1986. *Wea. Forecasting*, **14**, 687–700.
- McMurdie, L. A., and K. B. Katsaros, 1991: Satellite-derived integrated water-vapor distribution in oceanic midlatitude storms: Variation with region and season. *Mon. Wea. Rev.*, **119**, 589–605.

- Mendell, T., 1992: Integration of automated hydrological data. Preprints, *ASCE Conf. on Interdisciplinary Approaches in Hydrology and Hydrogeology*, Portland, OR, American Society of Civil Engineers. [Available from NOAA/California-Nevada River Forecast Center, 3310 El Camino Ave., Sacramento, CA 95821-6308.]
- Morss, R. E., and F. M. Ralph, 2007: Use of information by National Weather Service forecasters and emergency managers during CALJET and PACJET-2001. *Wea. Forecasting*, **22**, 539–555.
- Neiman, P. J., F. M. Ralph, A. B. White, D. E. Kingsmill, and P. O. G. Persson, 2002: The statistical relationship between upslope flow and rainfall in California's coastal mountains: Observations during CALJET. *Mon. Wea. Rev.*, **130**, 1468–1492.
- Palmén, E., and C. W. Newton, 1969: *Atmospheric Circulation Systems: Their Structure and Physical Interpretation*. Academic Press, 603 pp.
- Pandey, G. R., D. R. Cayan, and K. P. Georgakakos, 1999: Precipitation structure in the Sierra Nevada of California during winter. *J. Geophys. Res.*, **104**, 12 019–12 030.
- Ralph, F. M., P. J. Neiman, and G. A. Wick, 2004: Satellite and CALJET aircraft observations of atmospheric rivers over the eastern North Pacific Ocean during the winter of 1997/98. *Mon. Wea. Rev.*, **132**, 1721–1745.
- , —, and R. Rotunno, 2005: Dropsonde observations in low-level jets over the northeastern Pacific Ocean from CALJET-1998 and PACJET-2001: Mean vertical-profile and atmospheric-river characteristics. *Mon. Wea. Rev.*, **133**, 889–910.
- , —, G. A. Wick, S. I. Gutman, M. D. Dettinger, D. R. Cayan, and A. B. White, 2006: Flooding on California's Russian River: Role of atmospheric rivers. *Geophys. Res. Lett.*, **33**, L13801, doi:10.1029/2006GL026689.
- Rhea, J. O., 1978: Orographic precipitation model for hydrometeorological use. Ph.D. dissertation, Colorado State University, Dept. of Atmospheric Science Paper 287, 198 pp.
- Rotunno, R., and R. Ferretti, 2001: Mechanisms of intense alpine rainfall. *J. Atmos. Sci.*, **58**, 1732–1749.
- Schluessel, P., and W. J. Emery, 1990: Atmospheric water vapour over oceans from SSM/I measurements. *Int. J. Remote Sens.*, **11**, 753–766.
- Schneidereit, M., and C. Schär, 2000: Idealized numerical experiments of Alpine flow regimes and southside precipitation events. *Meteor. Atmos. Phys.*, **72**, 233–250.
- Smith, R. B., 1979: The influence of mountains on the atmosphere. *Advances in Geophysics*, Vol. 21, Academic Press, 87–230.
- Trabant, D. C., and G. P. Clagett, 1990: Measurement and evaluation of snowpacks. *Cold Regions Hydrology and Hydraulics*, W. L. Ryan and R. D. Crissman, Eds., American Society of Civil Engineers, 39–93.
- Waliser, D. E., and R. C. J. Somerville, 1994: Preferred latitudes of the intertropical convergence zone. *J. Atmos. Sci.*, **51**, 1619–1639.
- Weng, F., and N. C. Grody, 1994: Retrieval of cloud liquid water using the special sensor microwave imager. *J. Geophys. Res.*, **99**, 25 535–25 551.
- Wentz, F. J., 1997: A well-calibrated ocean algorithm for special sensor microwave/imager. *J. Geophys. Res.*, **102**, 8703–8718.
- Zhu, Y., and R. E. Newell, 1998: A proposed algorithm for moisture fluxes from atmospheric rivers. *Mon. Wea. Rev.*, **126**, 725–735.